

Production of Aromatics by Catalytic Fast Pyrolysis of Cellulose in a Bubbling Fluidized Bed Reactor

Pranav U. Karanjkar, Robert J. Coolman, and George W. Huber

Dept. of Chemical and Biological Engineering, University of Wisconsin-Madison, Madison, WI 53706

Michael T. Blatnik, Saba Almalkie, and Stephen M. de Bruyn Kops

Dept. of Mechanical Engineering, University of Massachusetts-Amherst, Amherst, MA 01003

Triantafillos J. Mountziaris and William C. Conner

Dept. of Chemical Engineering, University of Massachusetts-Amherst, Amherst, MA 01003

DOI 10.1002/aic.14376

Published online February 11, 2014 in Wiley Online Library (wileyonlinelibrary.com)

Catalytic fast pyrolysis of cellulose was studied at 500°C using a ZSM-5 catalyst in a bubbling fluidized bed reactor constructed from a 4.92-cm ID pipe. Inert gas was fed from below through the distributor plate and from above through a vertical feed tube along with cellulose. Flowing 34% of the total fluidization gas through the feed tube led to the optimal mixing of the pyrolysis vapors into the catalyst bed, which experimentally corresponded to 29.5% carbon aromatic yield. Aromatic yield reached a maximum of 31.6% carbon with increasing gas residence time by changing the catalyst bed height. Increasing the hole-spacing in the distributor plate was shown to have negligible effect on average bubble diameter and hence did not change the product distribution. Aromatic yields of up to 39.5% carbon were obtained when all studied parameters were optimized. © 2014 American Institute of Chemical Engineers AICHE J, 60: 1320–1335, 2014
 Keywords: biomass conversion, catalytic fast pyrolysis, gas–solid fluidization, K-L model

Introduction

Lignocellulosic biomass has attracted significant attention as a feedstock for production of renewable liquid fuels and valuable chemicals due to its low cost and abundance.^{1–19} Catalytic fast pyrolysis (CFP) allows the direct conversion of solid biomass into aromatics.^{20–25} CFP has numerous advantages compared to other approaches for biomass conversion because it can produce five major feedstocks that petroleum industry uses including benzene, toluene, xylene, ethylene, and propylene in a single step process that uses inexpensive zeolite catalysts.^{17,20,21,26–32} Toluene and xylenes may also be directly blended at high levels into gasoline and at low levels into distillate fuels. CFP of biomass is carried out in a fluidized bed reactor (FBR) where biomass is rapidly heated to high temperatures (450–650°C) where it forms oxygenated pyrolysis vapors.^{33–35} These vapors subsequently diffuse into the pores of the zeolite catalyst where they are converted to aromatics, olefins, CO, CO₂, and water. Coke is the major undesired byproduct that competes with aromatics formation.³⁶

ZSM-5 based catalysts exhibit the highest aromatic yields for CFP of biomass because of their pore size, low internal pore volume, and structure.^{26,37–42} The aromatic yield of CFP processes using ZSM-5 catalysts can be increased fur-

ther by the addition of metal oxides such as GaO and ZnO.^{43,44} The *p*-xylene selectivity can be increased while decreasing the coke yield by silylation of the catalyst so that over 90% of the xylenes are *p*-xylene.⁴⁵

Different feedstocks have been used for CFP including woods,^{20,21,26,27,46} grasses,⁴⁷ and model compounds.^{44,48} Jae et al. reported a maximum aromatic yield of 15.5% carbon from CFP of pine wood in a bubbling FBR using an unmodified spray-dried ZSM-5 catalyst, the same that is used in this study.⁴⁶ Plant biomass is composed of three main components—cellulose, hemicellulose, and lignin. It has been shown that cellulose primarily contributes toward aromatic production.^{49,50} Cellulose is a good model compound for raw woody biomasses because woods contain ~ 40% wt of cellulose. The pyrolysis of cellulose has been widely studied.^{36,51–56} The primary product of cellulose pyrolysis at temperatures of 400–600°C is levoglucosan which is formed by depolymerization of cellulose.⁵¹ Char, CO₂, and water are formed from cellulose pyrolysis at lower temperature.³⁶ Other products that are formed from cellulose pyrolysis include anhydrosugars, furans, light oxygenates, and noncondensable gases.^{51,53}

Several types of reactor configurations have been used for CFP including a microgram-scale resistively heated batch reactors, fixed bed reactors, and several FBR configurations including (1) bubbling fluidized beds, (2) spouting fluidized beds, and (3) circulating fluidized beds.^{20,26,27,48,57,58} FBRs are ideal for CFP because they allow for maintaining constant catalyst activity through continuous addition of fresh catalyst and removal of coked catalyst.⁴⁶ FBRs also provide

Additional Supporting Information may be found in the online version of this article.

Correspondence concerning this article should be addressed to G. W. Huber at huber@enr.wisc.edu.

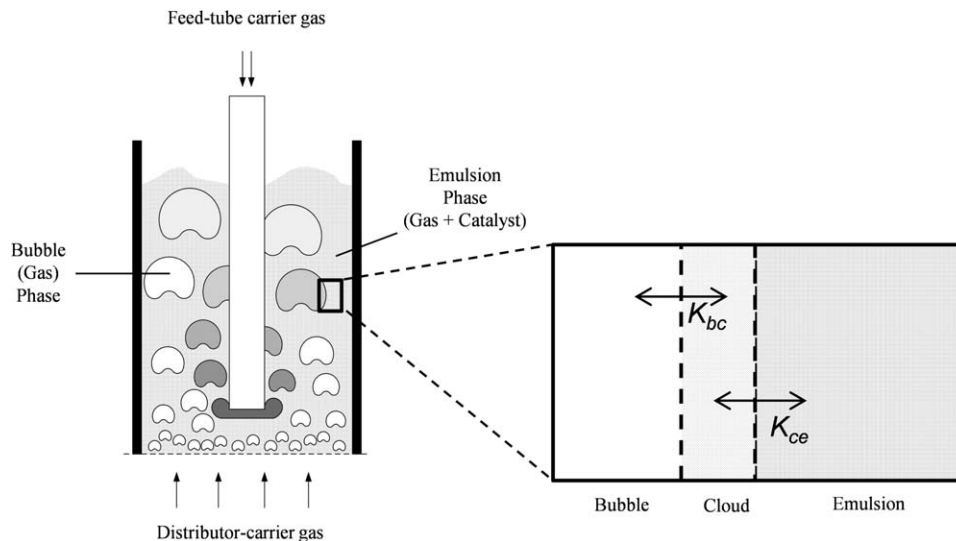


Figure 1. Schematic of a gas–solid FBR with two carrier gas inlets.

good heat transfer (for rapid heating of biomass) and good mass transfer (compared to other modes of gas–solid contacting). The absence of moving parts also makes FBRs ideal for CFP of biomass.^{59–61} The flow regime in which an FBR is operated depends on the fluidization velocity of the gas. We have previously reported that the production of aromatics by CFP of biomass is highest in a fluidized reactor that has a biomass weight hourly space velocity (WHSV) between 0.1 h^{-1} and 0.35 h^{-1} .^{20,46,62} These low space velocities can realistically only be achieved at an industrial scale by using reactor configurations with low void fractions, such as, bubbling beds ($\epsilon \approx 0.50$) or turbulent beds ($\epsilon \approx 0.70$). Fast-fluidized beds ($\epsilon \approx 0.90$) and pneumatic transport beds ($\epsilon > 0.99$) are not feasible at the desirable range of space velocities. For example, a 2000 metric ton of biomass feed per day reactor, at a WHSV of 0.3 h^{-1} requires 278 metric tons of catalyst, which at a density of 1250 kg m^{-3} , requires a solid volume of 222 m^3 . A 2-m diameter reactor with a void fraction typical of fast fluidization ($\epsilon = 0.96$), would require an implausible height of 1800 m.

Figure 1 shows a schematic of a bubbling FBR consisting of two phases: (1) a lean bubble phase containing mostly gas bubbles and (2) a well-mixed dense emulsion phase of solid catalyst particles and gas. At the minimum fluidization velocity, all the gas goes through the emulsion phase.⁶³ As the fluidization velocity increases above the minimum fluidization velocity, the gas in excess of minimum fluidization goes through the bubble phase. The bubble size increases with catalyst bed height as the bubbles coalesce. Between the bubble and emulsion phase, a cloud occurs wherein mass transfer takes place (see Figure 1).^{59,64–66} Understanding the hydrodynamics of this process is very important for the scale-up of CFP reactors, which is a relatively unexplored topic for CFP of biomass, as well as for elucidating the kinetics of this complex process and improving upon this technology.

The objective of this work is to study the CFP of cellulose in a FBR. We have collected data for CFP of cellulose under different hydrodynamic conditions and compared them with a hydrodynamic model to explain the evolution and role of bubbles. Compilation of various empirical models allowed

us to calculate hydrodynamic parameters including bed expansion, bubble diameter, and bubble residence time.

Experimental

Materials

Industrial-grade cellulose with an average particle size of $200 \mu\text{m}$ (Lattice® NT Microcrystalline Cellulose, FMC biopolymer, 99%) was used without pretreatment as the feedstock for this study. $\text{C}_6\text{H}_{10}\text{O}_5$ was used as an empirical formula for cellulose. The catalyst used in these experiments was a commercial spray-dried 40% ZSM-5 catalyst (Intercat) with an average particle size of $99 \mu\text{m}$ and a standard deviation of $23 \mu\text{m}$. Between 90 and 250 g of catalyst were loaded into the reactor. These loadings correspond to about 15–40% of the reactor volume. Prior to reaction, the catalyst was calcined *in situ* at 500°C in a mixture with a 1:4 oxygen-to-helium ratio flowing at 880 sccm. Equation 1 shows the WHSV of cellulose

$$\text{WHSV} (\text{h}^{-1}) = \frac{\text{cellulose flow rate} (\text{g} \cdot \text{h}^{-1})}{\text{weight of catalyst} (\text{g})} \quad (1)$$

The WHSV is calculated by dividing the cellulose flow rate by the amount of catalyst present inside the FBR. Selectivity toward a particular aromatic compound is defined by Eq. 2 obtained by dividing the number of moles of carbon in that aromatic product by the number of moles of carbon in all the aromatic products

Aromatic Selectivity

$$= \frac{\text{moles of carbon in an aromatic product}}{\text{moles of carbon in all aromatic products}} \times 100\% \quad (2)$$

Equation 3 defines the selectivity toward an olefin compound in a similar way

Olefin Selectivity

$$= \frac{\text{moles of carbon in an olefinic product}}{\text{moles of carbon in all olefinic products}} \times 100\% \quad (3)$$

As shown in Eq. 4, the residence time of the gas was calculated by dividing the catalyst bed volume by the total gas

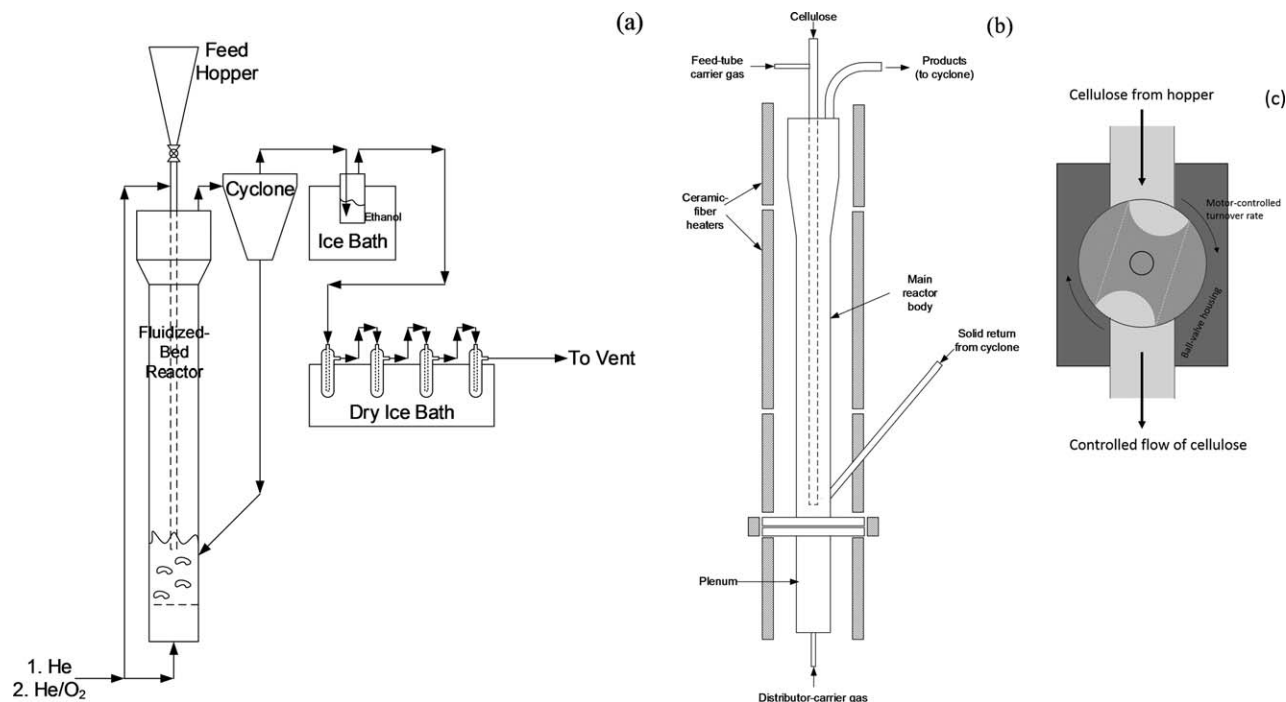


Figure 2. (a) Schematic of the experimental system, (b) detailed drawing of the reactor, and (c) diagram of feeder motor.

flow rate (Q_t) which is the sum of carrier gas flow rate (Q_c) and the product gas flow rate (Q_p)

Gas residence time (s)

$$= \frac{\text{Catalyst bed volume (cm}^3\text{)} \times 60 \text{ (s} \cdot \text{min}^{-1}\text{)}}{\text{Total gas flow rate (cm}^3 \cdot \text{min}^{-1}\text{)}} \quad (4)$$

Experimental setup

Figure 2 shows a schematic of the FBR system used for the CFP of cellulose. The FBR is a 316L stainless steel 4.92-cm ID pipe with a freeboard height of 40.64 cm. Above the freeboard is a disengaging zone which includes an expansion to a 7.79-cm ID pipe. The catalyst bed is supported by a distributor plate made of two layers of stainless steel perforated plates sandwiched around a 400 mesh stainless steel cloth. Cellulose is fed into the reactor via a feed hopper connected to a 1.10-cm ID feed tube entering from the top of the reactor and extending into the fluidized bed, ending at a height 1.52 cm above the distributor plate.

The free-fall time (0.35 s) of a particle is less than our lowest feed-tube gas residence time (6.3 s) in the feed tube. From Whitaker's correlation of convective heat transfer about a sphere,⁶⁷ it takes an upper bound of 0.1 s to heat the bulk of a 200- μm cellulose particle to 400°C in a 500°C stream of helium flowing at average freefall velocity. Based on pyrolysis rates determined by Cho et al.³⁶ pyrolysis of cellulose is extremely fast at 400°C (on the order of 0.1 g s⁻¹). It can, therefore, be assumed the 6 \times 10⁻⁶-gram cellulose particles are completely pyrolyzed upon exiting the feed tube.

As WHSV is an important parameter controlling the product yield and distribution,^{20,62} a feeder motor made from a partially filled ball valve is placed below the hopper (Figure 2c) to control the cellulose feed rate, thus controlling the

WHSV to within $\pm 2\%$ of the set value. During the reaction, catalyst particles were fluidized using a carrier stream of helium gas entering through the distributor (henceforth referred to as the distributor-carrier gas) and through the feed tube (henceforward referred to as the feed-tube carrier gas). This feed-tube carrier gas was necessary to ensure proper feeding of the cellulose into the fluidized bed. The gas flow rates were controlled by mass flow controllers (Brooks Instruments). The reactor was heated to the reaction temperature using four cylindrical ceramic-fiber heaters (WATLOW), each controlled separately to create a uniform temperature profile. The flanges joining the main reactor body and space beneath the distributor plate (henceforth referred to as the plenum) were heated using a band heater. Heating of the plenum allowed for preheating of the distributor-carrier gas to the reaction temperature before reaching the catalyst. A typical run was carried out over 30 min, during which, the products left the top of the reactor and entered a cyclone to separate any entrained catalyst particles which were then sent back to the reactor. The solid-free vapors were then bubbled through ethanol maintained at 0°C using an ice bath. Here, most organic species were captured through dissolution. The stream was then passed through four condensers maintained at -78°C using a dry-ice/acetone bath to condense remaining organics. The non-condensable gases were then either vented, plumbed through a soap-film flow meter, or sampled in tedlar gas-sampling bags (Restek) and analyzed using gas chromatography. After the reaction was completed, the reactor was flushed with helium for another 30 min to ensure complete purging of all volatile organic products. All of the contents of the ice bath (products dissolved in ethanol) and the condensers were then mixed together and analyzed using gas chromatography.

After purging, the reactor temperature was increased to 600°C, and the carrier gas was switched to an oxygen-helium mixture to combust char and coke in order to

regenerate the catalyst. For a typical run, the catalyst was regenerated for approximately 2 h to ensure complete combustion of any organic species remaining on the catalyst. The combustion effluent containing CO, CO₂, and water was passed through a copper catalyst (13% CuO on alumina, Sigma Aldrich) held at 250°C to convert CO to CO₂. This stream was then passed through a Dryrite trap to remove the water, followed by a preweighed Ascarite trap to capture CO₂ to determine the quantity of coke generated from the reaction through gravimetric analysis.^{62,68}

To test the reproducibility of results, we replicated experiments with varying catalyst bed height and varying distributor hole-spacing three times. We obtained standard deviation values of less than 3% for the carbon yields of different products which indicate that the data is reproducible and the trends discussed in the latter sections of this study are statistically significant.

Product analysis

After the reaction was completed, the liquid (mix of products dissolved in ethanol and products from condensers) was analyzed for aromatics using a Shimadzu GC2010 system with an Agilent HP INNOWax column (60 m, 0.32 mm, 0.5 μm) and a flame ionization detector (FID). The gaseous products collected at different times during the reaction were analyzed using a Shimadzu GC2014 system with (1) Restek Rtx®-VMS column (40 m, 0.25 mm, 1.5 μm) and an FID to analyze C3 and C4 olefins, and (2) a custom-made Supleco Hayesep D packed column with a thermal conductivity detector to analyze CO, CO₂, methane, and ethylene. Coke was measured using gravimetric analysis explained in Experimental Section. From carbon balance, unidentified carbon was calculated by subtracting moles of carbon in product from the moles of carbon in the cellulose feed. To calculate total mass balance in some of the experiments, water content in the liquid product was analyzed using a Mettler Toledo V20 compact volumetric Karl Fischer titrator.

Qualitative Computational Fluid Dynamics Simulations

Computational method

Preliminary simulations were conducted to determine the effect of two-inlet fluidization on the mixing of the fluidizing gas and the catalyst. Computational fluid dynamics (CFD) simulations were run on a simplified FBR with two gas inlets without the considerations of chemical reactions, heat or mass transfer, the cellulose biomass, or the size distribution of catalyst particles. The Eulerian-Eulerian two fluid model treats both the gas and solid phases as interpenetrating continua, each occupying a percent volume of the region of interest.⁶⁹ By continuity, the sum of these volume fractions is always equal to 1. The governing equations are based on conservation of mass, momentum, and energy for each phase.^{70–72}

CFD simulations were run on ANSYS® Fluent, Release 14.0, using a 2-D (two-dimensional) axi-symmetric mesh of 2.54-cm radius and 12.70-cm height with helium at 500°C as the primary fluidizing gas. For smaller Geldart Type A particles,⁶³ such as the ZSM-5 particles used in this study, Wang et al. have found that by using fine temporal and spatial resolutions (2 ≤ Δx ≤ 4d_p, where Δx is the mesh size and d_p is the particle diameter), small bubbles are

resolved and the correct bed expansion is achieved.^{73,74} Following these recommendations, the mesh size was set to ~ 30 cells/cm (3.39 × d_p) and the timestep was varied between Δt = 10⁻⁵ s and Δt = 10⁻⁴ s. The catalyst volume fraction (α) was initially set to 0.44 up to the height of the bed (5.77 cm, equivalent to 90-g catalyst), and to zero above the height of the bed. The catalyst volume fraction, granular temperature, energy, and the tracer gas conservation equations were solved using the QUICK numerical scheme and second-order time discretization was utilized due to the transient nature of the reactor.

Closure models are necessary to complete the conservation equations, many of which are semiempirically determined. In this work, a dense fluidized bed is assumed, which corresponds to the following closure models: granular temperature solved algebraically,⁷⁵ granular viscosity and drag model given by Gidaspow,⁶⁹ and granular bulk viscosity, solids pressure, and radial distribution function given by Lun.⁷⁶ The maximum solids volume fraction packing limit was set to 0.63. The frictional model comes from Johnson and Jackson with a friction packing limit of 0.60.⁷⁷ The reader is referred to van Wachem et al. for a more detailed description of the various closure models.⁷⁵

Quantifying mixing in CFD simulations

Tracer gases are commonly used to study how gas from a specific inlet mixes with the remainder of the bed by studying axial or radial tracer gas concentrations.^{78–81} To simulate the mixing of the pyrolysis vapors into the catalyst bed, we introduced inert tracer gases in Fluent. A 2 mol % nitrogen (N₂) gas was introduced at the bottom distributor-gas inlet and a 2 mol % argon (Ar) gas was introduced through the feed tube gas inlet. By studying the mixing of the argon from the feed tube gas with the nitrogen and helium gases and the catalyst (via mean and variance statistics), we can extract information on how the pyrolysis vapors would diffuse into the catalyst under CFP conditions.

Four statistical quantities (ε, ψ, θ, and φ) were calculated over the entire space of the catalyst bed and over a statistically steady time period (4 s) to inspect the mixing quality within the bed.⁸² The first is the mean void fraction ε = 1 - ⟨ᾱ⟩, the time-ensemble (denoted by ⟨X⟩, for some quantity X), volume-weighted (denoted by X̄) mean of the gas volume fraction, which measures the denseness of the bed. The normalized variance of the catalyst, ψ = ⟨α²⟩/α²_{max}, is a good measure of both the amount of bubbling within the bed and bed height fluctuations caused by high velocity gas streams. The catalyst statistics give insight into the fluidization of the catalyst, but, in order to identify how the feed tube gas mixes with this catalyst, we specifically calculate tracer gas statistics. To track the tracer gas mixing, the mixture fraction is utilized and defined as shown in Eq. 5

$$\zeta = \frac{Y_{N_2}^\infty - Y_{N_2}}{Y_{N_2}^\infty} \quad (5)$$

In Eq. 5, ζ = 1 at the feed tube gas inlet where the Ar tracer gas is at maximum concentration and ζ = 0 at the bottom gas inlet when there is no Ar tracer gas. The time-ensemble, volume-weighted mean of the mixture fraction scaled by the ideal mixture fraction, θ = ⟨ζ̄⟩/ζ̄_{ideal}, provides a good measure of how well the tracer gas is mixed. The ideal mixture fraction ζ̄_{ideal} is determined by substituting the outlet mass fraction of N₂ (Y_{N₂}^{outlet}) into Eq. 5 for Y_{N₂}.

Table 1. Comparison of Assemblage Model with K-L Model

| Symbol | Description | Assemblage Model | K-L Model |
|---------------|---|----------------------|-------------------------------|
| $d_{b,ave}$ | Average bubble diameter over the height of the bed (cm) | 1.19 (input for K-L) | Not predicted from this model |
| $u_{b,ave}$ | Average bubble rise velocity over the height of the bed (cm s ⁻¹) | 34.21 | 28.88 |
| δ | Fraction of the bed occupied by the bubble phase | 0.07 | 0.09 |
| L_f | Height of the fluidized bed (cm) | 18.44 | 18.72 |
| ε | Void fraction of the fluidized bed | 0.47 | 0.47 |
| τ_f | Average gas residence time in the fluidized bed (s) | 2.91 | 2.95 |
| τ_b | Gas residence time in the bubble phase (s) | 0.54 | 0.65 |
| τ_e | Gas residence time in the emulsion phase (s) | 18.18 | 18.18 |

A well-mixed bed represents a catalyst bed having tracer gas concentrations equivalent to outlet concentrations, and should thus have $\theta \approx 1$. The most important statistic used in quantifying the mixing potential of the feed tube gas is $\varphi = \frac{\langle \xi'^2 \rangle}{\langle \xi \rangle^2}$, the time-ensemble, volume-weighted variance of the mixture fraction, which is scaled by the mean mixture fraction squared. This quantity is equivalent to the squared coefficient of variation (standard deviation/mean) of the mixture fraction. Lower values of φ indicate better mixing of the feed tube gas as these represent cases with both a low variance of the feed tube gas (more uniformity of the tracer gas) within the reactor and a high amount of feed tube gas present within the catalyst.

Because of the assumptions stated in this section, the results from the CFD mixing quantification study only serve as a qualitative comparison to the experimental results. From the simulations, we look for trends in the mixing quality as measured by φ when altering the fraction of total carrier gas passing through the feed tube.

Literature-based Model for FBR

It was desired to gain an understanding of the hydrodynamics based on phenomena intrinsic to bubbling fluidized beds and the associated empirical relations found in the literature. For this, a model was constructed by combining these relations to enhance the understanding offered by more traditional treatments such as the Kunii-Levenspiel (K-L) model.

The most important hydrodynamic quantity is bubble size.⁸³ Although bubbles aid in turbulence and mixing, gas within bubbles must diffuse out into the surrounding emulsion phase to interact with the catalyst; to some extent, gas within a bubble bypasses the emulsion. Although there is appreciable gas exchange between the bubble and the emulsion, the mass-transfer rate is limited by the surface area of the bubble. Because the surface-area to volume ratio decreases as the bubbles coalesce, bubble-emulsion gas exchange rates decrease rapidly with increasing bubble size.

Many models of fluidized-bed hydrodynamics, including the K-L model, revolve around two-phase theory.⁵⁹ In two-phase theory, an “emulsion phase” is assumed to contain all particles and to be under the conditions of minimum fluidization (superficial velocity u_{mf} and void fraction ε_{mf}). All flow in excess of minimum fluidization is assumed to enter the “bubble phase,” which is assumed to be devoid of any particles. With these assumptions, it is possible to calculate a number of hydrodynamic quantities using only bubble rise velocity u_b and volume of solids V_s . These quantities include the fraction of the bed in the bubble phase δ , the height of the fluidized bed L_f , the overall void fraction of the fluidized bed ε , the average gas residence time τ_f , and the residence

times of the bubble- and emulsion-phases, τ_b and τ_e , respectively.

The K-L model uses the bubble size d_b as an input to calculate the bubble rise velocity u_b from an empirical model developed by Davidson et al.⁸⁴ Two-phase theory was subsequently used to calculate δ , L_f , ε , τ_f , τ_b , and τ_e . We developed a MATHCAD-based model by assembling a variety of empirical relations found in the literature. This model, herein referred to as the “assemblage model,” predicts the bubble size $d_b(z)$ and bubble rise velocity $u_b(z)$ as functions of the vertical distance above the distributor, z , using the inputs of bed mass, particle size, input fluidization gas velocity, and distributor configuration.⁵⁹ The model’s feasibility was verified through qualitative comparison with bubble sizes observed in a room-temperature transparent tube. Video footage of these bubbles can be found in Supporting Information. Other model results were validated by comparing predictions of the K-L model with the bubble size predicted by the assemblage model. Table 1 and Figure 3 compare the assemblage model to the K-L model.

A standard theory of two-phase fluidization was assumed. The emulsion phase was assumed to be at the point of minimum fluidization, and any gas flow in excess of minimum fluidization was assumed to enter the bubble phase. The minimum-fluidization velocity u_{mf} was determined from Eq. 6 as outlined by Wen and Yu⁸⁵

$$u_{mf} = \frac{\mu}{d_p \rho_g} \left(\sqrt{27.2^2 + 0.0408 \frac{d_p \rho_g \Delta \rho g}{\mu^2}} - 27.2 \right) \quad (6)$$

From here, the void fraction at minimum fluidization ε_{mf} was determined using Ergun’s equation shown in Eq. 7⁸⁶

$$\frac{d_p \rho_g (\Delta \rho) g}{\mu^2} = \frac{1.75}{\varepsilon_{mf}^3 \phi_s} \cdot \left(\frac{u_{mf} d_p \rho_g}{\mu} \right)^2 + \frac{150(1 - \varepsilon_{mf})}{\varepsilon_{mf}^3 \phi_s^2} \cdot \frac{u_{mf} d_p \rho_g}{\mu} \quad (7)$$

The volume of the emulsion phase was determined by dividing the volume of the solids V_s by the volume fraction of the emulsion phase shown in Eq. 8

$$V_e = \frac{V_s}{1 - \varepsilon_{mf}} \quad (8)$$

Equation 9 shows the residence time of the emulsion phase determined as the volume of the gas in this phase divided by its volumetric flow rate

$$\tau_e = \frac{\varepsilon_{mf} \cdot V_e}{(u_0 - u_{mf}) \cdot A_r} \quad (9)$$

The initial size of bubbles forming at the distributor was determined based on the fluidizing gas velocity u_0 and the spacing of the holes in the distributor l_{or} . The analysis is

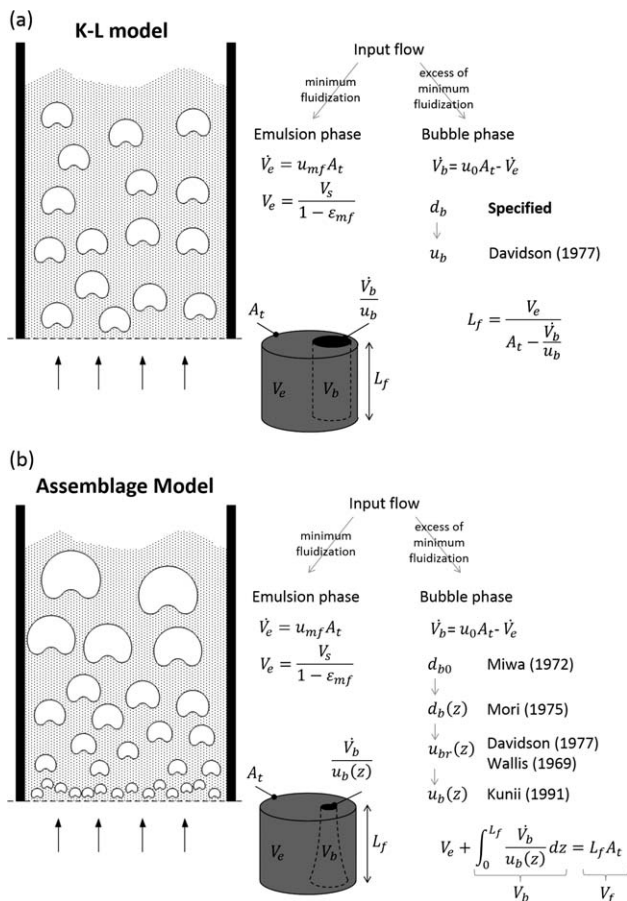


Figure 3. Illustrated demonstration of correlations used to construct the (a) K-L model and (b) assemblage model.

In the K-L model, a uniform bubble d_b size is specified to calculate all other hydrodynamic parameters (all which are also uniform throughout the fluidized bed). The assemblage model treats bubble size $d_b(z)$ and bubble rise velocity $u_b(z)$ as functions of distance above the distributor z and calculated averages for these quantities over a time-integrated basis.

described by Miwa et al.⁸⁷ and was modified by Kunii and Levenspiel.⁵⁹ The hole-density for a staggered arrangement of holes is given by Eq. 10

$$N_{or} = \frac{2}{\sqrt{3}l_{or}^2} \quad (10)$$

For initial bubble sizes smaller than hole-spacing l_{or} , the distributor was treated as a perforated plate and Eq. 11 was used to predict the initial bubble size

$$d_{b0,perforated} = \frac{1.3}{g^{0.2}} \left(\frac{u_0 - u_{mf}}{N_{or}} \right)^{0.4} \quad (11)$$

If the initial bubble size calculated from the perforated plate correlation $d_{b0,perforated}$ is larger than l_{or} , the distributor's behavior becomes indistinguishable from that of a porous plate. In this case, Eq. 12 is used in place of Eq. 11. The larger of the d_{b0} values obtained from Eqs. 11 and 12 was chosen for our analysis

$$d_{b0,porous} = \frac{2.78}{g} (u_0 - u_{mf})^2 \quad (12)$$

Bubble size increases as the bubbles coalesce. Bubble growth with respect to distance above the distributor is described by Mori and Wen⁶⁵ in Eq. 13. The diameter and cross-sectional area of the bed are denoted as D_t and A_t , respectively

$$d_b(z) = 0.65 \text{ cm} \cdot \left(\frac{A_t}{\text{cm}^2} \cdot \frac{u_0 - u_{mf}}{\text{cm} \cdot \text{s}^{-1}} \right)^{0.4} - \left(0.65 \text{ cm} \cdot \left(\frac{A_t}{\text{cm}^2} \cdot \frac{u_0 - u_{mf}}{\text{cm} \cdot \text{s}^{-1}} \right)^{0.4} - d_{b0} \right) \cdot \exp \left(\frac{-0.3 \cdot z}{D_t} \right) \quad (13)$$

The bubble size $d_b(z)$ was then used to determine the bubble-rise velocity with respect to the emulsion $u_{br}(z)$.⁸⁸ A graph showing the progress of bubble size $d_b(z)$ vs. a bubble's height above the distributor is shown in Figure 4a. For free bubbles, we used Eq. 14

$$u_{br,free}(z) = 0.711 \sqrt{g \cdot d_b(z)} \quad (14)$$

For bubble diameters exceeding 12.5% of D_t , the frictional effects of the walls were considered. Equation 15 accounts for the drag on bubbles by the walls⁸⁹

$$u_{br,wall}(z) = 0.711 \sqrt{g \cdot d_b(z)} \cdot 1.2 \cdot \exp \left(-1.49 \frac{d_b(z)}{D_t} \right) \quad (15)$$

We accounted for the emulsion's contribution to the movement of the bubbles from gulf-streaming. Kunii and Levenspiel⁵⁹ proposed Eq. 16 from Werther's data.⁹⁰ A graph showing the progress of bubble velocity $u_b(z)$ vs. a bubble's height above the distributor is shown in Figure 4b

$$u_b(z) = 1.55 \text{ m} \cdot \text{s}^{-1} \left(\frac{u_0 - u_{mf}}{\text{m} \cdot \text{s}^{-1}} + 14.1 \cdot \left(\frac{d_b(z)}{\text{m}} + 0.005 \right) \right) \cdot \left(\frac{D_t}{\text{m}} \right)^{0.32} + u_{br}(z) \quad (16)$$

Understanding the volumetric flow of the bubble phase to be a constant V_b , the bubble-rise velocity $u_b(z)$ was used to calculate a "cross-sectional area" of the bubble phase $A_b(z)$ by dividing V_b , by $u_b(z)$. The height of the bed L_f was found as the numerical value satisfying Eq. 17

$$V_e + \int_0^{L_f} A_b(z) dz = L_f A_t \quad (17)$$

The volume of the fluidized bed V_f was calculated as $L_f A_t$ and the volume of the bubble phase V_b was calculated as the difference $(V_f - V_e)$. The fraction of the bed in the bubble phase δ was calculated as V_b/V_f . The overall void fraction ϵ_f was calculated as $(V_f - V_s)/V_f$. The overall residence time τ_f was calculated as $\epsilon_f L_f / u_0$.

The bubble residence time τ_b was calculated as the time it takes a bubble to travel from $z = 0$ to $z = L_f$, as shown in Eq. 18

$$\tau_b = \int_0^{L_f} \frac{1}{u_b(z)} dz \quad (18)$$

For time-averaged hydrodynamic parameters, we numerically solved for the inverse function $z(t)$ from $t(z)$, shown by Eq. 19

$$t(z) = \int_0^z \frac{1}{u_b(h)} dh \quad (19)$$

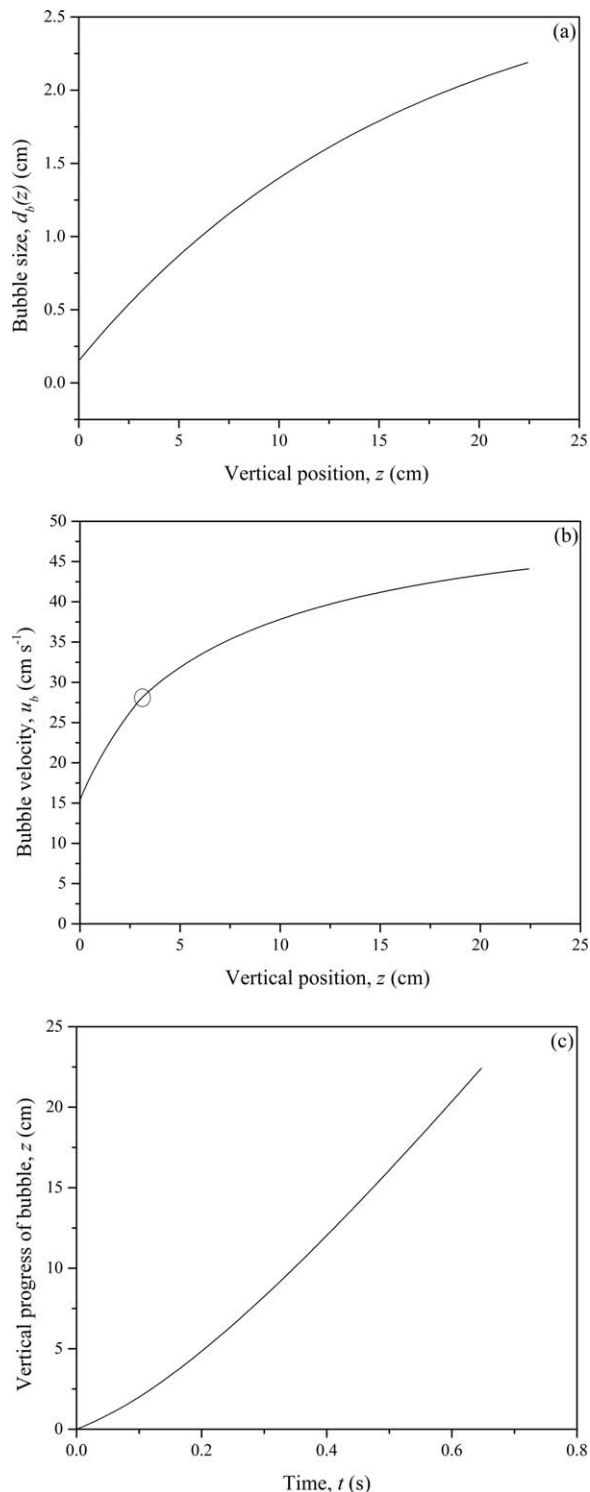


Figure 4. (a) Size of bubbles as a function of height above the distributor. Note the initial bubble size at $z = 0$. (b) The velocity of the bubbles as a function of height above the distributor. \circ indicates the transition from free bubbles to introduction of frictional wall effects. (c) The progress of a bubble's rise through the bed as a function of residence time.

Average bubble size $d_{b,ave}$ (Eq. 20) and average bubble velocity $u_{b,ave}$ (Eq. 21) were averaged over bubble residence time.

$$d_{b,ave} = \frac{1}{\tau_b} \int_0^{\tau_b} d_b(z(t)) dt \quad (20)$$

$$u_{b,ave} = \frac{1}{\tau_b} \int_0^{\tau_b} u_b(z(t)) dt \quad (21)$$

Figure 4c shows the vertical progress of a bubble as a function of time.

Results and Discussion

Determination of minimum fluidization velocity

The minimum fluidization velocity was determined experimentally using pressure drop measurements at the reaction temperature of 500°C as the molar flow rate of a carrier gas at the minimum fluidization is strongly dependent on temperature.^{91,92} The pressure drop across the bed vs. superficial gas velocity for decreasing velocities of helium is shown in Figure 5a. The pressure drop across the bed was calculated by subtracting the difference between the pressure drop of the reactor with the catalyst bed from the pressure drop of the empty reactor. These measurements are taken in the absence of flow through the feed-tube. The minimum fluidization velocity for the catalyst particles was found to be 0.36 cm s⁻¹ corresponding to a helium flow rate of 147 sccm (hereafter denoted as Q_{mf}). This minimum fluidization velocity value was found to be consistent with the predictions of both the CFD simulations and Eq. 6.^{85,93}

Figure 5b shows contour plots of the catalyst volume fraction for 10 different fluidizing velocities between $Q_c/Q_{mf} = 0.56$ and 8.33. At $Q_c/Q_{mf} < 1$, there are no changes in bed height or the catalyst volume fraction suggesting the bed is not fluidized at these velocities. When $1 < Q_c/Q_{mf} < 2.5$, we notice fairly uniform bed expansion with no bubbling. The lack of bubbling within the expansion stage is expected and in agreement with the characteristics of Geldart A particles, that bubbling occurs at a fluidizing velocity greater than the minimum fluidization velocity.⁶³ The minimum bubbling velocity can be determined both visually from the contour plots in Figure 5b (a few small bubbles at $Q_c/Q_{mf} = 2.78$ and more noticeable bubbles at $Q_c/Q_{mf} = 4.17$) and quantitatively by analyzing the increase in the bars showing the standard deviation of the inlet pressure in time when $Q_c/Q_{mf} = 4.17$ in Figure 5a. We thus define the point of minimum bubbling as $Q_c/Q_{mf} = 4$. The minimum bubbling velocity u_{mb} is defined in terms of the bottom distributor plate fluidizing velocity u_f such that $u_{mb} = 1.44$ cm s⁻¹.

Effect of total carrier gas flow rate

CFP of cellulose was carried out at different values of the total flow rate of carrier gas (Q_c) while holding the WHSV and amount of catalyst in the bed constant. The total flow rate of carrier gas is the sum of distributor-carrier and feed-tube carrier gases. The fraction of the total amount of gas passed through the feed tube was kept constant ($Q_{ft}/Q_c = 0.34$). Figures 6a, b and Table 2 show product yields as a function of this total carrier gas flow rate while other parameters such as bed temperature, cellulose WHSV, and catalyst-bed mass were kept constant. Table 2 also lists the bubble residence time and average gas residence times inside the catalyst bed. Gas residence time was calculated using Eq. 4. The total gas flow rate (Q_c) includes the product gas flow rate (Q_p) as the latter was measured to be in the range of 300 to 350 sccm for the cellulose WHSV of 0.24 h⁻¹

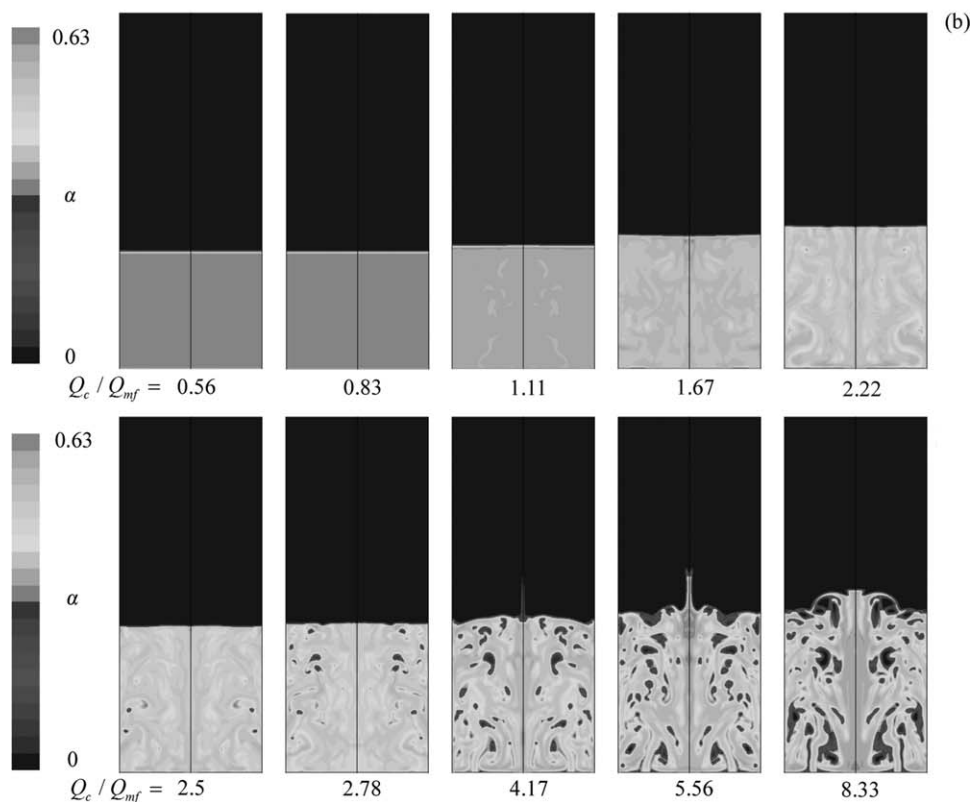
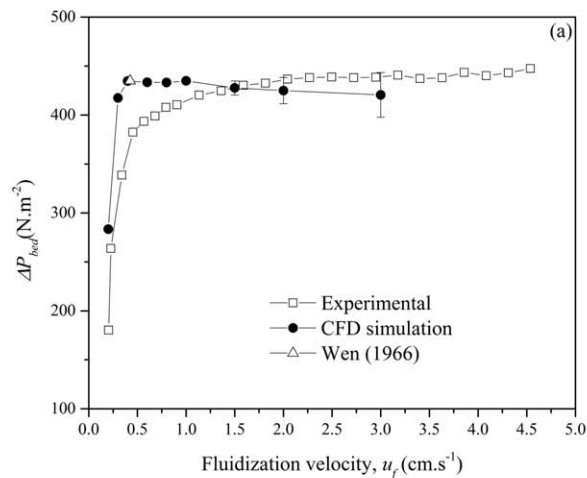


Figure 5. (a) Pressure drop across the catalyst bed vs. fluidization velocity at 500°C (error bars on the CFD simulation results show two standard deviations in time above and below the mean inlet pressure). (b) Contour plots for catalyst volume fraction vs. fluidization velocity from simulations.

(with 250 g of catalyst). As Q_c/Q_{mf} increased, the average gas residence time decreased from 9.95 to 5.61 s in a slightly indirect proportion. This deviation due to the fact that as the total carrier gas flow rate is increased, the catalyst bed expands and contributes slightly to an increase in gas residence time. As shown in Figure 6a, the aromatic yield went through a maximum of 39.5% carbon which occurred at an intermediate value of gas and bubble residence time corresponding to four times the minimum fluidization flow rate. The unidentified hydrocarbons showed the exact opposite trend and gave a minimum carbon yield of 13.3% carbon at four times the minimum fluidization flow rate. We have shown previously that the unidentified carbon consists of molecular weight oligomer species (including tars) that

collect in the condensers or elsewhere in the system. Mass balances of up to 85 wt % were achieved by analyzing the water content of the liquid product. The remaining 15 wt % is most likely high molecular weight species. In previous experiments, we have been able to obtain mass balance of 100 wt % \pm 10 wt %. We have shown that in the case of using water (instead of ethanol) in the condenser train, these unidentified species are found in the bubbler in the form of a floating black residue.⁴⁶ The carbon yields of C_2 – C_4 olefins did not exhibit a particular trend with respect to carrier gas flow rate. The maximum olefin yield was 4.8% carbon.

The aromatic yield for CFP of cellulose is about twice the aromatic yield for CFP of pine wood.^{20,46} The coke yields for CFP of pine wood are 30–35% carbon, which are 2–3

times higher than coke yields obtained in this work from CFP of cellulose. The cellulose portion of the biomass thus contributes more to the aromatics than the other components of the biomass. These results are consistent with the work of Jae et al.⁴⁹ where they observed that for maple wood, maple wood with hemicellulose extracted, and maple wood with cellulose and hemicellulose extracted, aromatic yield decreased with increasing lignin content. These work suggest that lignin and the ash content in the biomass are detrimental to the production of aromatics and different feedstocks will have a different aromatics yield depending on the composition of the biomass feedstock.

Effect of distribution of carrier gas from distributor plate and feed tube

To study the mixing of cellulose pyrolysis vapors into the fluidized catalyst bed, the fraction of the total amount of carrier gas passing through the feed tube was changed from ~ 8 to ~ 70%, whereas the total carrier gas flow rate (feed tube flow rate plus distributor gas flow rate as shown on Figures 1 and 2) was maintained constant ($Q_c/Q_{mf} = 7.6$). Table 3 and Figures 7a, b show the product yields as a function of

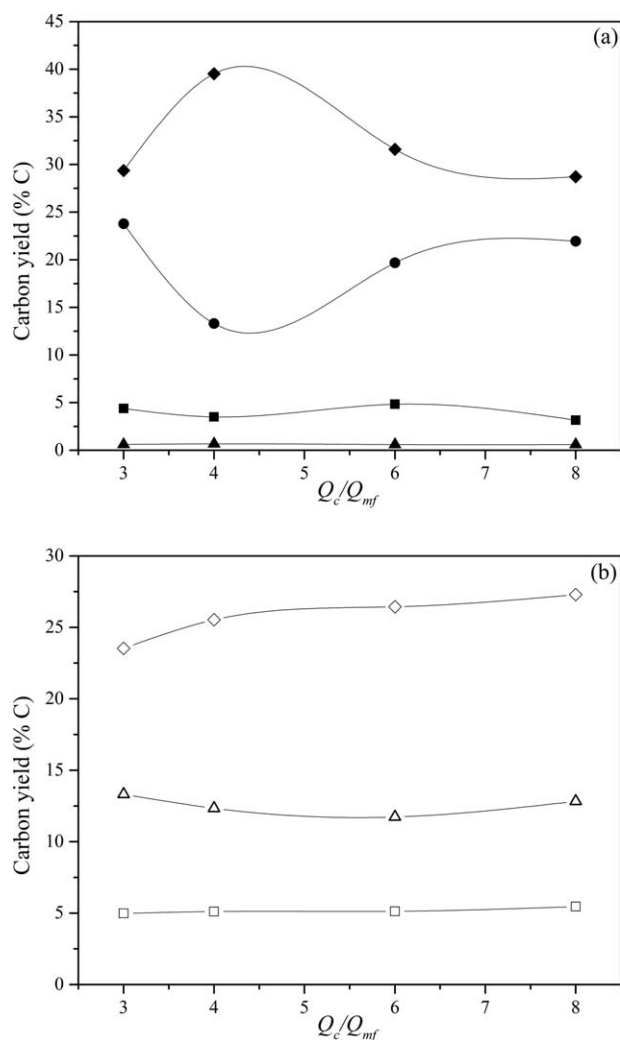


Figure 6. Product yields as a function of Q_c/Q_{mf} at 500°C, $Q_{ft}/Q_c = 0.34$ and $WHSV = 0.25 \pm 0.02 \text{ h}^{-1}$. Key: (a) \blacklozenge Aromatics, \blacksquare C2-C4 olefins, \blacktriangle Methane, \bullet Unidentified (b) \diamond CO, \square CO₂, \triangle coke.

Table 2. Detailed Product Yields and Selectivities for CFP of Cellulose at Various Flow Rates of Carrier Gas as a Multiplier of the Minimum Fluidization Flow Rate

| Parameters | Q_c/Q_{mf} | | | |
|--|--------------|-------|-------|-------|
| | 3 | 4 | 6 | 8 |
| d_b (cm) | 0.68 | 0.80 | 1.01 | 1.18 |
| u_b (cm s ⁻¹) | 20.64 | 22.85 | 26.24 | 28.97 |
| δ | 0.04 | 0.05 | 0.08 | 0.10 |
| L_f (cm) | 19.65 | 19.93 | 20.44 | 20.89 |
| τ_b (s) | 0.95 | 0.87 | 0.80 | 0.72 |
| $(L_f - L_m)/L_m$ | 0.12 | 0.13 | 0.16 | 0.19 |
| Q_t (sccm) | 797 | 934 | 1191 | 1502 |
| τ_f (s) | 9.95 | 8.61 | 6.93 | 5.61 |
| Overall Yields (% carbon) | | | | |
| Aromatics | 29.4 | 39.5 | 31.6 | 28.7 |
| C ₂ -C ₄ Olefins | 4.4 | 3.5 | 4.8 | 3.2 |
| Methane | 0.6 | 0.7 | 0.6 | 0.6 |
| CO | 23.5 | 25.5 | 26.4 | 27.3 |
| CO ₂ | 5.0 | 5.1 | 5.1 | 5.5 |
| Coke | 13.3 | 12.3 | 11.7 | 12.8 |
| Total carbon balance | 76.2 | 86.7 | 80.3 | 78.0 |
| Unidentified | 23.8 | 13.3 | 19.7 | 22.0 |
| Aromatic Selectivity | | | | |
| Benzene | 17.0 | 20.4 | 17.8 | 17.6 |
| Toluene | 33.6 | 36.7 | 34.9 | 35.7 |
| Ethyl-benzene | 0.83 | 0.81 | 0.64 | 0.71 |
| Xylenes | 21.3 | 20.5 | 20.9 | 22.3 |
| Styrene | 0.0 | 0.2 | 0.2 | 0.0 |
| Benzofuran | 0.4 | 0.2 | 0.2 | 0.4 |
| Indene | 2.5 | 2.1 | 2.6 | 0.3 |
| Phenol | 2.3 | 1.5 | 1.8 | 2.4 |
| Naphthalenes | 22.0 | 17.6 | 20.8 | 20.7 |
| Olefin Selectivity | | | | |
| Ethylene | 36.9 | 51.4 | 42.0 | 67.8 |
| Propylene | 55.5 | 43.6 | 52.3 | 28.2 |
| C ₄ olefins | 7.6 | 5.0 | 5.7 | 4.0 |

Reaction conditions: Temperature of bed: 500°C, $Q_{ft}/Q_c = 0.34$, and $WHSV \sim 0.25 \pm 0.02 \text{ h}^{-1}$ with 250 g catalyst.)

fraction of the carrier gas that was passed through the feed tube. The aromatic yield went through a maximum of 29.5% carbon that occurred when 34% of total carrier gas was passed through the feed tube. At the same point the yield of unidentified products went through a minimum of 18.4% carbon. The coke yield also went through a maximum with a change in the fraction of carrier gas passing through the feed tube. The other products did not show a large systematic change with a change in the fraction of carrier gas passing through the feed tube. This data indicates the importance of mixing of cellulose pyrolysis vapors coming through the feed tube into the fluidized catalyst bed. This is further supported by simulations.

Figure 8 shows the catalyst volume fraction contour plots, the argon tracer gas mass fraction, and the catalyst axial velocity from CFD simulations run with different values of Q_{ft}/Q_c . From Figure 8a, we note that the $Q_{ft}/Q_c = 8, 18,$ and 34% cases have similar α profiles with about the same bed height. The latter two cases of $Q_{ft}/Q_c = 52$ and 69% , however, show a marked difference with lower bed height, a denser bed, and spouts of particles along the feeding tube. We do not observe significant bubbling when $Q_{ft}/Q_c = 52$ and 69% . In Figure 8b, the Ar feed tube tracer gas can be seen as mostly uniform within the bed for the three lower Q_{ft}/Q_c cases, and, in contrast, nonuniform for the two higher cases. The flow of the catalyst reverses direction along the feed tube wall (see Figure 8c) when a specific transition point is reached (between $Q_{ft}/Q_c = 34$ and 52%), which as

Table 3. Detailed Product Yields and Selectivities for CFP of Cellulose at Various Velocities of Carrier Gas through the Feed Tube

| Parameters | Fraction of Carrier Gas Passing Through Feed Tube | | | | |
|--|---|------|------|------|------|
| | 0.08 | 0.18 | 0.34 | 0.52 | 0.69 |
| ε | 0.58 | 0.59 | 0.58 | 0.56 | 0.54 |
| ψ | 0.18 | 0.18 | 0.19 | 0.20 | 0.24 |
| θ | 0.91 | 0.90 | 0.88 | 0.67 | 0.60 |
| φ | 0.24 | 0.16 | 0.12 | 0.18 | 0.28 |
| u_f (cm s ⁻¹) | 2.55 | 2.27 | 1.83 | 1.33 | 0.86 |
| Overall Yields (% carbon) | | | | | |
| Aromatics | 23.6 | 26.5 | 29.5 | 25.5 | 23.7 |
| C ₂ –C ₄ Olefins | 5.1 | 6.8 | 5.5 | 5.1 | 5.3 |
| Methane | 0.9 | 0.7 | 0.7 | 0.6 | 0.9 |
| CO | 24.1 | 26.4 | 28.6 | 26.3 | 28.7 |
| CO ₂ | 5.0 | 5.3 | 5.3 | 5.1 | 5.7 |
| Coke | 10.6 | 11.2 | 12.2 | 12.3 | 11.6 |
| Total carbon balance | 69.3 | 76.9 | 81.6 | 75.0 | 76.0 |
| Unidentified | 30.7 | 23.1 | 18.4 | 25.0 | 24.0 |
| Aromatic Selectivity | | | | | |
| Benzene | 16.0 | 17.3 | 15.4 | 17.1 | 16.2 |
| Toluene | 35.5 | 37.8 | 34.4 | 36.8 | 35.4 |
| Ethyl-benzene | 1.3 | 1.5 | 1.3 | 1.4 | 0.0 |
| Xylenes | 28.2 | 20.4 | 21.9 | 22.0 | 22.4 |
| Styrene | 0.0 | 3.1 | 0.4 | 2.2 | 1.2 |
| Benzofuran | 0.2 | 0.3 | 1.3 | 0.3 | 2.2 |
| Indene | 3.1 | 2.8 | 0.7 | 3.1 | 1.0 |
| Phenol | 1.8 | 2.2 | 9.5 | 2.1 | 11.1 |
| Naphthalenes | 13.9 | 14.6 | 15.0 | 15.1 | 10.5 |
| Olefin Selectivity | | | | | |
| Ethylene | 38.9 | 41.1 | 41.6 | 39.3 | 39.7 |
| Propylene | 55.8 | 54.1 | 52.2 | 55.3 | 52.9 |
| C ₄ olefins | 5.3 | 4.8 | 6.2 | 5.4 | 7.4 |

Reaction conditions: Temperature of bed: 500°C, WHSV: 0.51 ± 0.04 h⁻¹ with 90 g catalyst, $Q_c/Q_{mf} = 7.6$.)

seen in Table 3, occurs when the fluidization velocity u_f passes below u_{mb} .

Figure 7c reveals that the average void fraction (ε) is roughly constant in all five cases, which implies that the void fraction is primarily a function of the total flow rate Q_c . The normalized variance of the catalyst volume fraction (ψ) increases slightly when increasing Q_{ft}/Q_c primarily due to increased fluctuation in the bed height. Figure 7c also shows that θ is close to 1 for the first three cases ($Q_{ft}/Q_c = 8, 18,$ and 34%) indicating an ideally mixed reactor. The variance of the mixture fraction divided by the mean mixture fraction squared, φ goes through a minimum value of 0.12 at $Q_{ft}/Q_c = 34\%$, suggesting that this is the point for optimal mixing of the pyrolysis vapors into the catalyst bed. This point exactly corresponds to the maximum aromatic yield obtained experimentally. These results show that designing the biomass feed injector system so that the biomass effectively gets well mixed into the FBR is critical for obtaining high aromatic yields during CFP of biomass.

The CFD simulations in this study are for a simplified two-inlet fluidized bed. These simulations show qualitative trends regarding the mixing of the feed tube gas with the catalyst. The u_{mb} and bubble residence time were not determined experimentally and thus, it is unknown whether the CFD simulations are predicting the correct point of bubbling within the reactor vs. fluidizing velocity. Additional research that can provide validation to the simulations would be to experimentally determine the u_{mb} and bubble residence time.

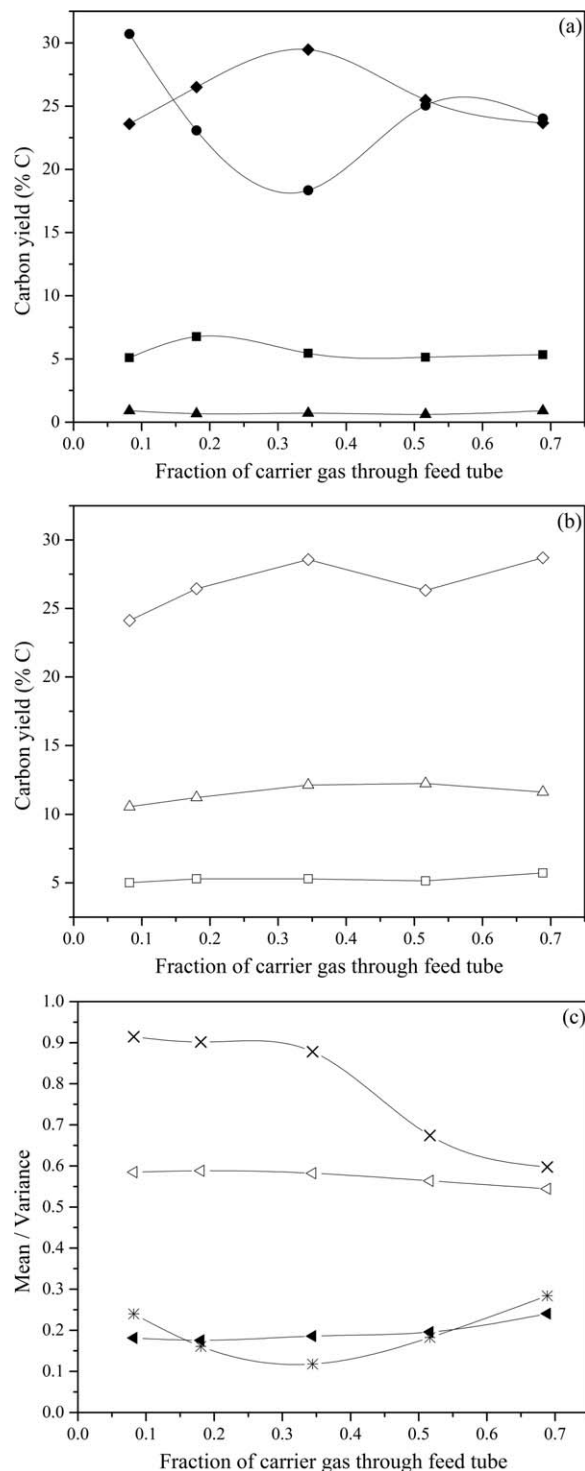


Figure 7. Product yields as a function of gas velocity through feed tube at 500°C, $Q_c/Q_{mf} = 7.6$, and $WHSV = 0.51 \pm 0.04$ h⁻¹. Key: (a) \blacklozenge Aromatics, \blacksquare C₂–C₄ olefins, \blacktriangle Methane, \bullet Unidentified (b) \diamond CO, \square CO₂, \triangle coke (c) \triangleleft ε , \blacktriangleleft ψ , \times θ , $*$ φ .

Ensuring that the u_{mb} is similar for both the experiment and the simulations gives credence to the theory that the best mixing (and thus, the highest aromatic yields) occurs when u_f is at or just above u_{mb} , as was noticed with the simulations.

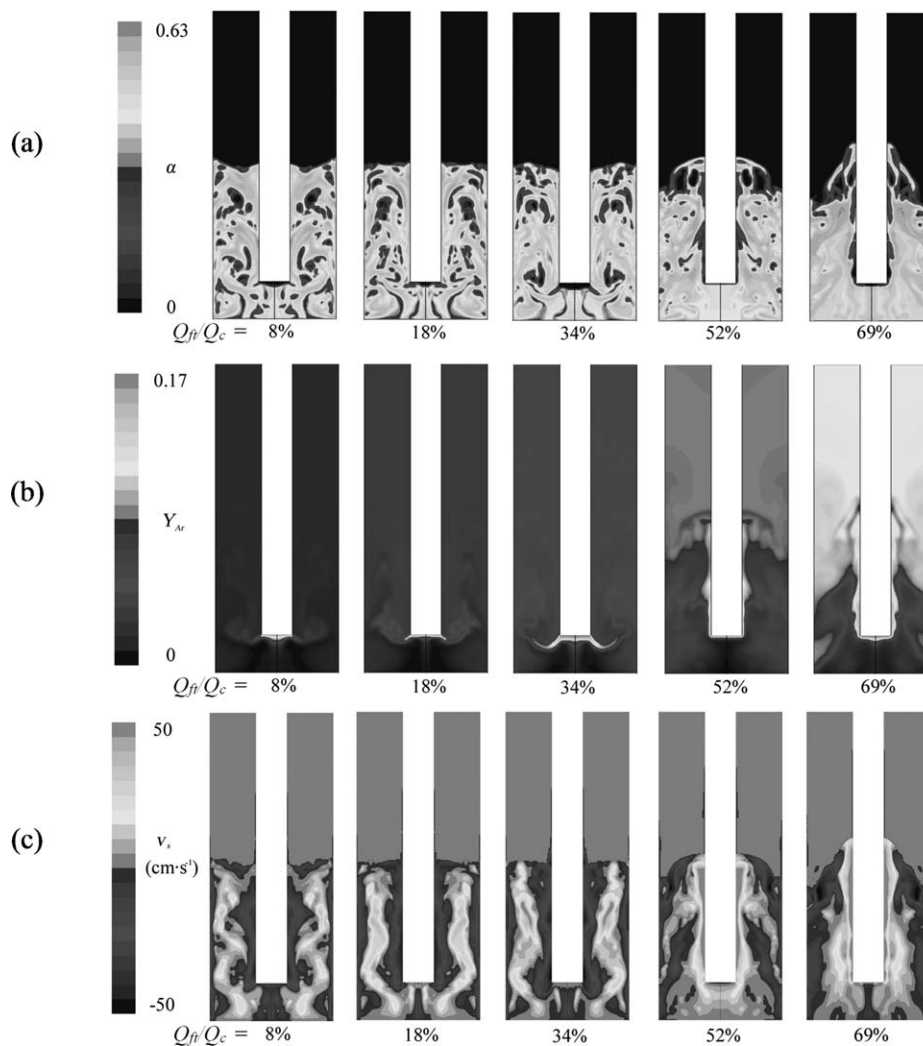


Figure 8. Contour plots from simulation (increasing feed tube fraction of carrier gas left-to-right) of (a) catalyst volume fraction (α), (b) mass fraction of Ar tracer gas entering from the feed tube (Y_{Ar}), and (c) axial velocity of the catalyst (v_s).

Effect of catalyst bed height

Figure 9 and Table 4 show the product yield as a function of the catalyst bed height for CFP of cellulose at a bed temperature of 500°C and cellulose WHSV of 0.24 h^{-1} . Each of these experiments were replicated 3 times to confirm the reproducibility of the results and standard deviations were calculated which are reported in Table 4. A typical standard deviation of 1–2% was calculated for the product yields and distribution. Table 4 reports calculated fluidized bed height (L_f) for different amounts of catalysts. The cellulose flow rate was increased with increasing bed height to maintain a constant WHSV. This increase in WHSV led to an increase in the product gas flow rate. The total carrier gas inlet flow rate was held constant for all of these experiments. The increase in the bed size leads to an increase in bubble residence time (τ_b) and gas residence time (τ_f). The bubble residence time and gas residence time increased from 0.36 to 0.69 s and 3.07 to 7.22 s, respectively. Initially, as the bed height increased from 6.4 to 12 cm, the aromatic yield increased from 27.6% carbon to 31.5% carbon. Further increase in bed height to 17.6 cm only increased the aro-

matic yield by 0.1% carbon. The aromatic selectivity, however, did change with increased bed height. The benzene and toluene selectivities decreased from 20.2 and 37.4 to 17.8 and 34.9%, respectively, as the bed height increased. The naphthalenes selectivity increased from 13.7 to 20.8% with increased bed height, suggesting that gas residence time is an important parameter for tuning selectivity toward monoaromatics. The selectivity towards oxygenates such as benzofuran and phenol also showed a slight decrease with an increase in bed height. This could be because of the longer gas residence time in the catalyst bed allowing for more deoxygenation by decarbonylation and decarboxylation. This is consistent with the slight increase in CO and CO₂ yield. The yield of C₂–C₄ olefins increased from 3.7 to 4.8% with slightly higher selectivity towards C₃–C₄ olefins than ethylene. Among other noncondensable gases, CO and CO₂ showed an overall increase in their yields. The coke yield decreased from 14.3 to 11.7% as the bed height increased. These results suggest that gas residence time plays an important role in tuning the product distribution. Higher gas residence times shift the aromatics distribution toward polyaromatic compounds.

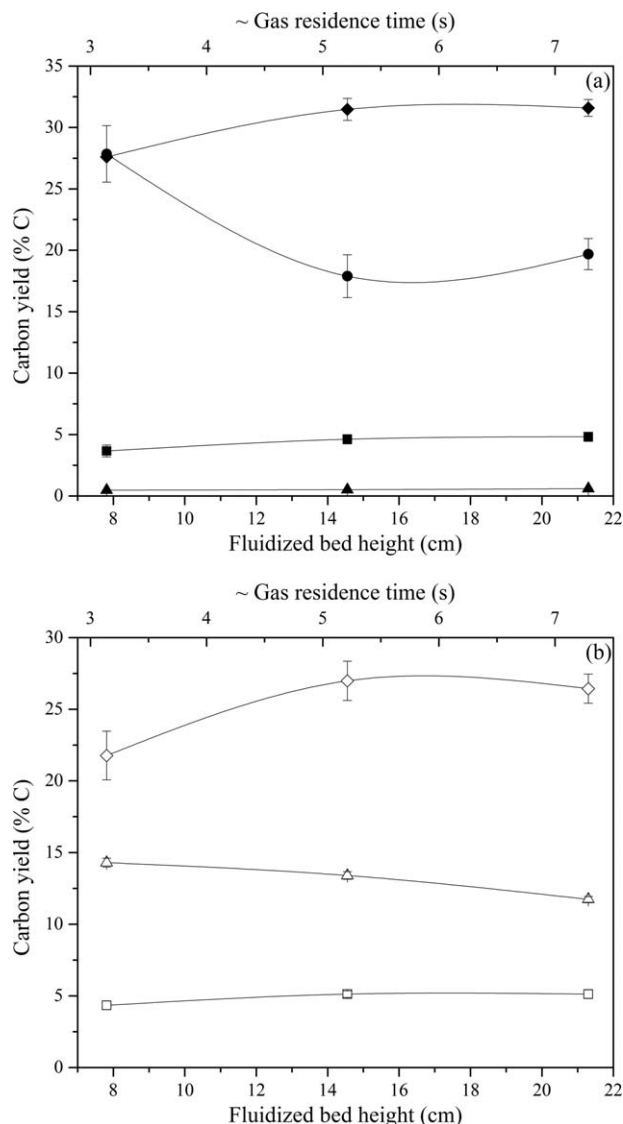


Figure 9. Product yields as a function of catalyst bed height/bubble residence time at 500°C, $Q_c/Q_{mf} = 6$, and $WHSV = 0.24 \pm 0.02 \text{ h}^{-1}$. Key: (a) \blacklozenge Aromatics, \blacksquare C2–C4 olefins, \blacktriangle Methane, \bullet Unidentified (b) \diamond CO, \square CO₂, \triangle coke.

In these experiments, as the cellulose WHSV is maintained at a constant value of 0.25 h^{-1} , increasing the bed height also increases the rate at which cellulose is fed. This changes the concentration of pyrolysis vapors entering into the catalyst bed from the feed-tube. It is not known whether this increase of local concentration of pyrolysis vapors at the outlet of the feed-tube significantly affects the product distribution independently of residence time.

Effect of distributor plate hole-spacing

Three distributor plates were prepared with different hole-spacings: 284, 787, and 2778 μm . Hole-spacing is the center-to-center distance between two holes on a distributor. As described in Product analysis Section, hole-spacing of a distributor plate determines the initial diameter of the bubbles formed. The experiments were carried out at a constant temperature of 500°C, a constant WHSV of 0.24 h^{-1} , and a fixed carrier gas flow rate of 880 sccm. Each experiment was repeated 3 times to test the reproducibility of the results.

We expected a significant difference in the product yield as a function of the initial bubble diameter, which was varied over an order of magnitude. Table 5 shows the hydrodynamic parameters calculated using the assemblage model developed here. Although initial bubble size was estimated to increase by an order of magnitude when similarly increasing the distributor hole spacing, other hydrodynamic parameters (most importantly, average bubble size) were estimated to remain almost constant. This was reflected in the product distribution. Table 5 and Figure 10 show product yields with standard deviations as a function of hole-spacing in a perforated plate distributor plate. Standard deviations of less than 1% for the product yields are indication of reproducible results. The bubble residence time was estimated to change slightly from 0.73 to 0.69 s with a change in the distributor plate. The gas residence time did not change in this case as the product flow rate was almost the same in all the experiments. The aromatic yield and C₂–C₄ olefins showed only a slight change as the hole-spacing was increased almost 10 times. As can be seen from Table 5, the yield and selectivity of different products did not change appreciably. As the average bubble diameter did not change appreciably, we were unable to test the effect of average bubble size on the product distribution.

Because distributor hole spacing did not change the bubble size at this scale, it was hypothesized that, for average bubble size, the effect of bubble coalescence dominates over the effect of initial bubble size. To test this hypothesis, the

Table 4. Detailed Product Yields and Selectivities for CFP of Cellulose for Different Catalyst Bed Heights

| Parameters | Bed Height (cm) | | |
|--|-----------------|------------|------------|
| | 7.81 | 14.55 | 21.30 |
| Catalyst amount (g) | 90 | 170 | 250 |
| d_b (cm) | 0.66 | 1.02 | 1.34 |
| u_b (cm s ⁻¹) | 21.93 | 26.93 | 30.78 |
| δ | 0.11 | 0.10 | 0.09 |
| τ_b (s) | 0.36 | 0.54 | 0.69 |
| $(L_r - L_m)/L_m$ | 0.23 | 0.22 | 0.21 |
| Q_t (sccm) | 1026 | 1100 | 1191 |
| τ_r (s) | 3.07 | 5.34 | 7.22 |
| Overall yields (% carbon) | | | |
| Aromatics | 27.6 ± 0.1 | 31.5 ± 0.9 | 31.6 ± 0.7 |
| C ₂ –C ₄ Olefins | 3.7 ± 0.5 | 4.6 ± 0.4 | 4.8 ± 0.4 |
| Methane | 0.5 ± 0.0 | 0.5 ± 0.0 | 0.6 ± 0.0 |
| CO | 21.8 ± 1.7 | 27.0 ± 1.4 | 26.4 ± 1.0 |
| CO ₂ | 4.3 ± 0.3 | 5.1 ± 0.2 | 5.1 ± 0.3 |
| Coke | 14.3 ± 0.3 | 13.4 ± 0.3 | 11.7 ± 0.2 |
| Total carbon balance | 72.2 | 82.1 | 80.3 |
| Unidentified | 27.9 ± 2.3 | 17.9 ± 1.7 | 19.7 ± 1.3 |
| Aromatic Selectivity | | | |
| Benzene | 20.2 ± 0.8 | 18.4 ± 0.2 | 17.8 ± 0.2 |
| Toluene | 37.4 ± 1.0 | 35.5 ± 0.2 | 34.9 ± 0.4 |
| Ethyl-benzene | 0.8 ± 0.1 | 0.5 ± 0.0 | 0.6 ± 0.0 |
| Xylenes | 20.9 ± 0.0 | 20.9 ± 0.1 | 20.9 ± 0.1 |
| Styrene | 1.0 ± 0.2 | 0.3 ± 0.1 | 0.2 ± 0.1 |
| Benzofuran | 0.5 ± 0.1 | 0.3 ± 0.1 | 0.2 ± 0.0 |
| Indene | 3.2 ± 0.2 | 2.7 ± 0.1 | 2.6 ± 0.0 |
| Phenol | 2.2 ± 0.4 | 1.9 ± 0.1 | 1.8 ± 0.1 |
| Naphthalenes | 13.7 ± 1.1 | 19.5 ± 0.2 | 20.8 ± 0.6 |
| Olefin Selectivity | | | |
| Ethylene | 46.5 ± 2.6 | 46.2 ± 3.4 | 42.0 ± 0.3 |
| Propylene | 49.3 ± 2.6 | 49.4 ± 3.1 | 52.3 ± 0.5 |
| C ₄ olefins | 4.3 ± 0.1 | 4.3 ± 0.4 | 5.72 ± 0.4 |

Reaction Conditions: Temperature of bed: 500°C, WHSV: $0.24 \pm 0.02 \text{ h}^{-1}$, $Q_c/Q_{mf} = 6$.)

Table 5. Detailed Product Yields and Selectivities for CFP of Cellulose for Different Hole-Spacing in the Distributor Plates

| Parameters | Hole-Spacing (μm) | | |
|--|--------------------------------|----------------|----------------|
| | 284 | 787 | 2778 |
| d_{b0} (cm) | 0.02 | 0.06 | 0.15 |
| d_b (cm) | 1.21 | 1.24 | 1.34 |
| u_b (cm s ⁻¹) | 29.34 | 29.74 | 30.78 |
| δ | 0.10 | 0.10 | 0.09 |
| L_f (cm) | 21.41 | 21.38 | 21.30 |
| τ_b (s) | 0.73 | 0.72 | 0.69 |
| $(L_f - L_m)/L_m$ | 0.22 | 0.22 | 0.21 |
| Q_r (sccm) | 1191 | 1191 | 1191 |
| τ_f (s) | 7.26 | 7.25 | 7.22 |
| Overall Yields (% carbon) | | | |
| Aromatics | 30.9 \pm 0.6 | 31.9 \pm 0.7 | 31.6 \pm 0.7 |
| C ₂ –C ₄ Olefins | 4.4 \pm 0.3 | 4.7 \pm 0.2 | 4.8 \pm 0.4 |
| Methane | 0.7 \pm 0.0 | 0.7 \pm 0.0 | 0.6 \pm 0.0 |
| CO | 28.7 \pm 0.3 | 27.6 \pm 1.0 | 26.4 \pm 1.0 |
| CO ₂ | 5.4 \pm 0.7 | 5.4 \pm 0.1 | 5.1 \pm 0.3 |
| Coke | 13.0 \pm 0.2 | 12.4 \pm 0.2 | 11.7 \pm 0.2 |
| Total carbon balance | 83.2 | 82.8 | 80.3 |
| Unidentified | 16.8 \pm 1.3 | 17.3 \pm 0.4 | 19.7 \pm 1.3 |
| Aromatic Selectivity | | | |
| Benzene | 17.8 \pm 0.5 | 16.6 \pm 0.4 | 17.8 \pm 0.2 |
| Toluene | 34.0 \pm 0.7 | 34.5 \pm 0.5 | 34.9 \pm 0.4 |
| Ethyl-benzene | 0.6 \pm 0.1 | 0.6 \pm 0.0 | 0.6 \pm 0.0 |
| Xylenes | 20.2 \pm 0.8 | 21.3 \pm 0.4 | 20.9 \pm 0.1 |
| Styrene | 0.3 \pm 0.0 | 0.4 \pm 0.2 | 0.2 \pm 0.1 |
| Benzofuran | 0.2 \pm 0.0 | 0.3 \pm 0.0 | 0.2 \pm 0.0 |
| Indene | 2.4 \pm 0.2 | 2.5 \pm 0.3 | 2.6 \pm 0.1 |
| Phenol | 1.7 \pm 0.2 | 1.9 \pm 0.4 | 1.8 \pm 0.1 |
| Naphthalenes | 22.6 \pm 1.5 | 22.0 \pm 1.1 | 20.8 \pm 0.6 |
| Olefin Selectivity | | | |
| Ethylene | 45.9 \pm 5.8 | 42.1 \pm 2.2 | 42.0 \pm 0.3 |
| Propylene | 48.9 \pm 6.0 | 52.7 \pm 2.0 | 52.3 \pm 0.5 |
| C ₄ olefins | 5.2 \pm 0.4 | 5.2 \pm 0.3 | 5.7 \pm 0.4 |

Reaction Conditions: Temperature of bed: 500°C, WHSV: 0.24 \pm 0.01 h⁻¹ with 250 g catalyst, Q_c/Q_{mf} = 6.)

assemblage model was tested at larger scales. The results are shown in Table 6. From the results, we see that distributor-hole spacing only affects the average bubble size in a small way, and that this effect becomes more pronounced at larger scales. This suggests that coalescence is a more important phenomenon to average bubble size than initial bubble size, and this effect of coalescence is more important at smaller scales.

Future CFD Work

As our results show that hydrodynamics of FBRs is likely to play an important role in scale up of the CFP technology, there is a need for a more in-depth study on the hydrodynamics of the FBRs for CFP. Because of the various assumptions involved, the simulations presented in this work can only show qualitative trends for a general FBR with two gas inlets. Future work for CFD simulations can include further validation and verification of the numerical model. The 2-D-axisymmetric assumption must be tested against a full three-dimensional (3-D) simulation. Statistical quantities, such as ϵ , ψ , θ , and ϕ , as well as hydrodynamic quantities, such as the bubble rise velocity, size, and residence time, would need to be compared for both the 2-D and the 3-D case to determine if the 2-D-axisymmetric assumption is sufficient. The 3-D case could also be used to achieve a more

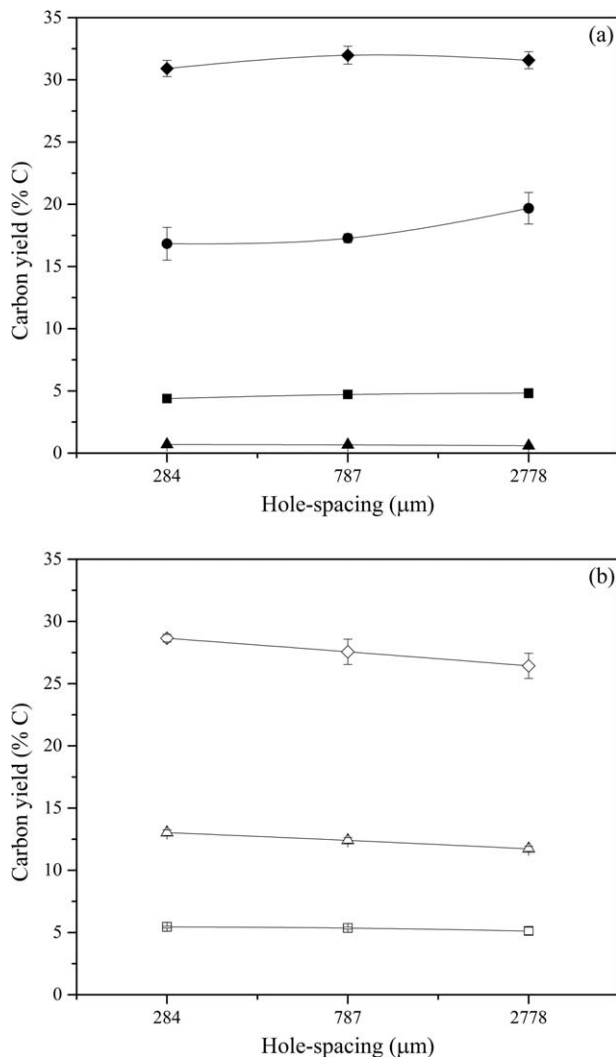


Figure 10. Product yields as a function of hole-spacing in the distributor plate at 500°C, Q_c/Q_{mf} = 6, and WHSV = 0.24 \pm 0.01 h⁻¹. Key: (a) ◆ Aromatics, ■ C₂–C₄ olefins, ▲ Methane, ● Unidentified (b) ◇ CO, □ CO₂, △ coke.

complete and accurate description of the bed's hydrodynamics. Sensitivity analysis studies for the various closure models such as the drag model, particle–particle frictional stress model, and the particle viscosity model, for the Eulerian–Eulerian simulation method could be performed to better match the simulations to experiment. Furthermore, sensitivity analysis with regard to the numerical methods, mesh size, and time steps, will also need to be performed to provide verification to the simulations. Lastly, adding chemical

Table 6. Results Obtained from the Assemblage Model at Different Scales

| Parameters | Hole-Spacing (μm) | | |
|--|--------------------------------|------|------------|
| | 284 | 2778 | % increase |
| d_{b0} (cm) | 0.02 | 0.15 | 650.00% |
| Average bubble size for $D_t = 5$ cm | 1.07 | 1.20 | 12.15% |
| Average bubble size for $D_t = 50$ cm | 0.91 | 1.07 | 17.58% |
| Average bubble size for $D_t = 500$ cm | 0.63 | 0.77 | 22.22% |

To maintain bed height (~ 21 cm) the mass of bed particles was varied proportionally to the square of the column diameter D_t .

reactions, mass and heat transfer, and cellulose to the simulations is a future step that would ensure a complete numerical model.

Conclusions

We carried out CFP of cellulose in a bubbling FBR. We obtained a maximum of 39% carbon yield of aromatics from cellulose as compared to reported values of 15.5% carbon yield from CFP of pine wood. This indicates that most of the aromatics formed from biomass during CFP come from the cellulose portion of the biomass. This also suggests that the lignin component of the biomass decreases the aromatics yield.

We found that the mixing between the catalyst and the biomass feed is a function of the amount of fluidization gas that is fed through the distributor plate vs. from the feed tube (which comes into the reactor with the solid cellulose feed). CFD simulations showed that bubbling was achieved only when the velocity of fluidization gas through the distributor plate (u_f) exceeded the minimum bubbling velocity (u_{mb}). The preliminary CFD simulations provided a qualitative way to study the mixing of the carrier gas coming through the feed tube into the fluidized catalyst bed. To study this mixing, we introduced inert tracer gases in simulations and calculated the mixture fraction scaled by the ideal mixture fraction (θ) and the variance of mixture fraction over the mean mixture fraction squared (φ). Higher values of θ and lower values of φ indicate better mixing of the pyrolysis vapors into the fluidized bed. The experimental aromatics yield was higher when the simulation results indicated better mixing. The aromatics yield is maximized with the mixing between the cellulose pyrolysis vapors and the catalyst bed and FBRs should be designed to maximize this mixing. These results illustrate the importance of properly designing the mixing point between the biomass feed and the catalyst bed in CFP reactors.

Using the assemblage model, we calculated hydrodynamic parameters and compared them against the experimental product yields to elucidate the effects of bubble hydrodynamics on the reaction. Average bubble sizes were predicted not to change significantly and no trends were observed between product yield and bubble size. Further use of the assemblage model suggested that the resolution of this model for hydrodynamic effects intrinsic to bubbles is too low to observe in our experimental reactor. However, these effects are likely to become more important at larger scales. This lack of resolution was confirmed experimentally, as no significant trends were observed when changing the hole-spacing on the distributor plate.

We used different catalyst bed heights to study how bubble residence time and gas residence time affect product yields. The aromatic yield increased from 27.6% carbon at a bed height of 6.4 cm to 31.6% carbon at a bed height of 17.6 cm. The monocylic aromatic selectivity was higher at lower bed heights. Thus, for a bubbling FBR, gas residence time is an important parameter for tuning the aromatic product distribution.

Acknowledgments

This work was funded by the National Science Foundation Office of Emerging Frontiers in Research and Innovation (EFRI) grant number 0937895. High performance computing resources were provided by the US Department of Defense High Performance Computing Modernization Program at the Army Research Laboratory (ARL) and at the Army Engineer

Research and Development Center (ERDC). Professor G.W. Huber has an ownership interest in Anellotech, which has licensed the technology reported in this publication.

Notation

$A_b(z)$ = area of cross-section occupied by bubbles at height z , cm^2
 d_{b0} = initial bubble diameter, cm
 d_{bm} = maximum bubble diameter, cm
 d_b = bubble diameter, cm
 $d_{b,ave}$ = average bubble diameter, cm
 d_p = catalyst particle diameter, μm
 D_f = diameter of the FBR, cm
 L_f = fluidized bed height, cm
 L_m = minimum/fix bed height, cm
 l_{or} = hole-spacing in a distributor plate, cm
 \dot{m}_i = mass flow rate of species i at inlet j , $\text{g}\cdot\text{s}^{-1}$
 N_{or} = hole-density of a distributor plate, cm^{-2}
 Q_c = total carrier gas flow rate, sccm
 Q_{ft} = carrier gas flow rate through feed tube, sccm
 Q_{mf} = minimum fluidization flow rate, sccm
 Q_p = products flow rate, sccm
 Q_t = total gas flow rate, $\text{sccm} = Q_c + Q_p$
 u_0 = Superficial velocity of the carrier gas, cm s^{-1}
 u_b = bubble velocity, cm s^{-1}
 $u_{b,ave}$ = average bubble velocity, cm s^{-1}
 u_f = velocity of gas through the bottom inlet, cm s^{-1}
 u_{mb} = minimum bubbling velocity, cm s^{-1}
 u_{mf} = minimum fluidization velocity, cm s^{-1}
 V_i = volume of phase i , cm^3
 \dot{V}_i = volumetric flow of phase i , $\text{cm}^3 \text{s}^{-1}$
 v_s = axial component of the catalyst velocity, cm s^{-1}
 Y_i^∞ = free stream mass fraction of species i , dimensionless
 Y_i = mass fraction of component i , dimensionless
 z = height above the distributor plate, cm

Greek letters

α = catalyst volume fraction, dimensionless
 δ = fraction of bed occupied by bubble phase, dimensionless
 ε = void fraction, dimensionless
 θ = mixture fraction percentage from CFD, dimensionless
 ζ = mixture fraction, dimensionless
 ζ_{ideal} = ideal mixture fraction, dimensionless
 ρ_i = density of component i , g cm^{-3}
 τ_b = gas residence time in bubble phase, s
 τ_e = gas residence time in emulsion phase, s
 τ_f = overall vapor residence time in fluidized bed, s
 φ = variance of mixture fraction parameter from CFD, dimensionless
 ψ = variance of catalyst volume fraction parameter from CFD, dimensionless

Literature Cited

- Lappas AA, Iliopoulou EF, Kalogiannis K. Catalysts in biomass pyrolysis. In: Crocker M, editor. *Thermochemical Conversion of Biomass to Liquid Fuels and Chemicals*. Vol. 1. 2010:263–287.
- Lynd NR, Wyman CE, Gerngross TU. Biocommodity engineering. *Biotechnol Prog*. 1999;15(5):777–793.
- Wyman CE. Biomass ethanol: technical progress, opportunities, and commercial challenges. *Annu Rev Energy Environ*. 1999;24:189–226.
- Wyman CE, Dale BE, Elander RT, Holtzapple M, Ladisch MR, Lee YY. Coordinated development of leading biomass pretreatment technologies. *Bioresour Technol*. 2005;96:1959–1966.
- Singh NR, Delgass WN, Ribeiro FH, Agrawal R. Estimation of liquid fuel yields from biomass. *Environ Sci Technol*. 2010;44(13):5298–5305.
- Roman-Leshkov Y, Barrett CJ, Liu ZY, Dumesic JA. Production of dimethylfuran for liquid fuels from biomass-derived carbohydrates. *Nature*. 2007;447(7147):982–985.
- Chheda JN, Huber GW, Dumesic JA. Liquid-phase catalytic processing of biomass-derived oxygenated hydrocarbons to fuels and chemicals. *Angew Chem Int Ed Engl*. 2007;46(38):7164–7183.

8. Huber GW, Chheda JN, Barrett CJ, Dumesic JA. Production of liquid alkanes by aqueous-phase processing of biomass-derived carbohydrates. *Science*. 2005;308(5727):1446–1450.
9. Davda RR, Shabaker JW, Huber GW, Cortright RD, Dumesic JA. A review of catalytic issues and process conditions for renewable hydrogen and alkanes by aqueous-phase reforming of oxygenated hydrocarbons over supported metal catalysts. *Appl Catal B*. 2005;56:171–186.
10. Huber GW, Iborra S, Corma A. Synthesis of transportation fuels from biomass: chemistry, catalysts and engineering. *Chem Rev*. 2006;106:4044–4098.
11. Williams CL, Chang C-C, Do P, Nikbin N, Caratzoulas S, Vlachos DG, Lobo RF, Fan W, Dauenhauer PJ. Cycloaddition of biomass-derived furans for catalytic production of renewable p-xylene. *ACS Catal*. 2012;2(6):935–939.
12. Wright M, Brown RC. Comparative economics of biorefineries based on the biochemical and thermochemical platforms. *Biofuels Bioprod Bioref*. 2007;1:191–200.
13. Patwardhan PR, Brown RC, Shanks BH. Understanding the fast pyrolysis of lignin. *ChemSusChem*. 2011;4(11):1629–1636.
14. Czernik S, French R, Feik C, Chornet E. Hydrogen by catalytic steam reforming of liquid byproducts from biomass thermoconversion processes. *Ind Eng Chem Res*. 2002;41:4209–4215.
15. Czernik S, Scahill J, Diebold J. The production of liquid fuel by fast pyrolysis of biomass. *J Sol Energy Eng Trans ASME*. 1995;117(1):2–6.
16. Bridgwater AV. Review of fast pyrolysis of biomass and product upgrading. *Biomass Bioenergy*. 2012;38:68–94.
17. Lappas AA, Samolada MC, Iatridis DK, Voutetakis SS, Vasalos IA. Biomass pyrolysis in a circulating fluid bed reactor for the production of fuels and chemicals. *Fuel*. 2002;81(16):2087–2095.
18. Huber GW, Corma A. Synergies between bio- and oil refineries for the production of fuels from biomass. *Angew Chem Int Ed Engl*. 2007;46(38):7184–7201.
19. Huber GW, O'Connor P, Corma A. Processing biomass in conventional oil refineries: production of high quality diesel by hydrotreating vegetable oils in heavy vacuum oil mixtures. *Appl Catal A Gen*. 2007;329:120–129.
20. Carlson TR, Cheng Y-T, Jae J, Huber GW. Production of green aromatics and olefins by catalytic fast pyrolysis of wood sawdust. *Energy Environ Sci*. 2011;4:145–161.
21. Carlson TR, Vispute TP, Huber GW. Green gasoline by catalytic fast pyrolysis of solid biomass compounds. *ChemSusChem*. 2008;1:397–400.
22. Huber GW, Cheng Y-T, Carlson TR, Vispute T, Jae J, Tompsett GA. Inventors, University of Massachusetts, assignee. Catalytic pyrolysis of solid biomass and related biofuels, aromatics, and olefin compounds, 2009.
23. Zhang H, Cheng Y-T, Vispute TP, Xiao R, Huber GW. Catalytic conversion of biomass-derived feedstocks into olefins and aromatics with ZSM-5: the hydrogen to carbon effective ratio. *Energy Environ Sci*. 2011;4(6):2297–2307.
24. Zhang H, Xiao R, Jin B, Shen D, Chen R, Xiao G. Catalytic fast pyrolysis of straw biomass in an internally interconnected fluidized bed to produce aromatics and olefins: effect of different catalysts. *Bioresour Technol*. 2013;137:82–87.
25. Zhang H, Xiao R, Jin B, Xiao G, Chen R. Biomass catalytic pyrolysis to produce olefins and aromatics with a physically mixed catalyst. *Bioresour Technol*. 2013;140:256–262.
26. Aho A, Kumar N, Eraenen K, Salmi T, Hupa M, Murzin DY. Catalytic pyrolysis of woody biomass in a fluidized bed reactor: influence of the zeolite structure. *Fuel*. 2008;87(12):2493–2501.
27. Olazar M, Aguado R, Bilbao J, Barona A. Pyrolysis of sawdust in a conical spouted-bed reactor with a HZSM-5 catalyst. *AIChE J*. 2000;46(5):1025–1033.
28. Carlson TR, Tompsett GA, Conner WC, Huber GW. Aromatic production from catalytic fast pyrolysis of biomass-derived feedstocks. *Top Catal*. 2009;52:241–252.
29. Pattiya A, Titiloye JO, Bridgwater AV. Fast pyrolysis of cassava rhizome in the presence of catalysts. *J Anal Appl Pyrolysis*. 2008;81(1):72–79.
30. French R, Czernik S. Catalytic pyrolysis of biomass for biofuels production. *Fuel Process Technol*. 2010;91(1):25–32.
31. Diebold J, Scahill J. Biomass to gasoline - upgrading pyrolysis vapors to aromatic gasoline with zeolite catalysis at atmospheric-pressure. *ACS Symp Ser*. 1988;376:264–276.
32. Bridgwater AV. Upgrading biomass fast pyrolysis liquids. *Environ Prog Sustain Energy*. 2012;31(2):261–268.
33. Lin Y-C, Cho J, Tompsett GA, Westmorland PR, Huber GW. Kinetics and mechanism of cellulose pyrolysis. *J Phys Chem C*. 2009;113(46):20097–20107.
34. Dauenhauer PJ, Colby JL, Balonek CM, Suszynski WJ, Schmidt LD. Reactive boiling of cellulose for integrated catalysis through an intermediate liquid. *Green Chem*. 2009;11(10):1555–1561.
35. Mettler MS, Vlachos DG, Dauenhauer PJ. Top ten fundamental challenges of biomass pyrolysis for biofuels. *Energy Environ Sci*. 2012;5(7):7797–7809.
36. Cho J, Davis JM, Huber GW. The intrinsic kinetics and heats of reactions for cellulose pyrolysis and char formation. *ChemSusChem*. 2010;3:1162–1165.
37. Foster AJ, Jae J, Cheng YT, Huber GW, Lobo RF. Optimizing the aromatic yield and distribution from catalytic fast pyrolysis of biomass over ZSM-5. *Appl Catal A Gen*. 2012;423:154–161.
38. Adjaye JD, Bakhshi NN. Production of hydrocarbons by catalytic upgrading of a fast pyrolysis bio-oil. Part II: comparative catalyst performance and reaction pathways. *Fuel Process Technol*. 1995;45(3):185–202.
39. Adjaye JD, Bakhshi NN. Production of hydrocarbons by catalytic upgrading of a fast pyrolysis bio-oil. Part I: conversion over various catalysts. *Fuel Process Technol*. 1995;45(3):161–183.
40. Bridgwater AV, Cottam ML. Opportunities for biomass pyrolysis liquids production and upgrading. *Energy Fuels*. 1992;6(2):113–120.
41. Aho A, Kumar N, Eraenen K, Salmi T, Hupa M, Murzin DY. Catalytic pyrolysis of biomass in a fluidized bed reactor: influence of the acidity of H-beta zeolite. *Process Saf Environ Prot*. 2007;85(B5):473–480.
42. Jae J, Tompsett GA, Foster AJ, Hammond KD, Auerbach SM, Lobo RF, Huber GW. Investigation into the shape selectivity of zeolite catalysts for biomass conversion. *J Catal*. 2011;279:257–268.
43. Cheng Y-T, Jae J, Shi J, Fan W, Huber GW. Production of renewable aromatic compounds by catalytic fast pyrolysis of lignocellulosic biomass with bifunctional ga/zsm-5 catalysts. *Angew Chem*. 2012;124(6):1416–1419.
44. Fanchiang W-L, Lin Y-C. Catalytic fast pyrolysis of furfural over H-ZSM-5 and Zn/H-ZSM-5 catalysts. *Appl Catal A Gen*. 2012;419:102–110.
45. Cheng Y-T, Wang Z, Gilbert CJ, Fan W, Huber GW. Production of p-xylene from biomass by catalytic fast pyrolysis using zsm-5 catalysts with reduced pore openings. *Angew Chem Int Ed Engl*. 2012;51(44):11097–11100.
46. Jae J, Coolman R, Mountziaris TJ, Huber GW. Catalytic fast pyrolysis of lignocellulosic biomass in a process development unit with continual catalyst addition and removal. *Chem Eng Sci*. 2014;108:33–46.
47. Wu X, Markham J, Sun XS, Wang D. Optimizing catalytic fast pyrolysis of biomass for hydrocarbon yield. *Trans ASABE*. 2012;55(5):1879–1885.
48. Cheng Y-T, Huber GW. Chemistry of furan conversion into aromatics and olefins over HZSM-5: a model biomass conversion reaction. *ACS Catal*. 2011;1(6):611–628.
49. Jae J, Tompsett GA, Lin Y-C, Carlson TR, Shen J, Zhang T, Yang B, Wyman CE, Conner WC, Huber GW. Depolymerization of lignocellulosic biomass to fuel precursors: maximizing carbon efficiency by combining hydrolysis with pyrolysis. *Energy Environ Sci*. 2010;3:358–365.
50. Wang K, Kim KH, Brown RC. Catalytic pyrolysis of individual components of lignocellulosic biomass. *Green Chem*. 2014.
51. Lin Y-C, Cho J, Tompsett GA, Westmoreland PR, Huber GW. Kinetics and mechanism of cellulose pyrolysis. *J Phys Chem C*. 2009;113(46):20097–20107.
52. Mettler MS, Mushrif SH, Paulsen AD, Javadekar AD, Vlachos DG, Dauenhauer PJ. Revealing pyrolysis chemistry for biofuels production: conversion of cellulose to furans and small oxygenates. *Energy Environ Sci*. 2012;5(1):5414–5424.
53. Mettler MS, Paulsen AD, Vlachos DG, Dauenhauer PJ. The chain length effect in pyrolysis: bridging the gap between glucose and cellulose. *Green Chem*. 2012;14(5):1284–1288.
54. Antal MJ, Varhegyi G. Cellulose pyrolysis kinetics: the current state of knowledge. *Ind Eng Chem Res*. 1995;34:703–717.
55. Antal MJ, Várhegyi G, Jakab E. Cellulose pyrolysis kinetics: revisited. *Ind Eng Chem Res*. 1998;37:1267–1275.

56. Patwardhan PR, Satrio JA, Brown RC, Shanks BH. Product distribution from fast pyrolysis of glucose-based carbohydrates. *J Anal Appl Pyrolysis*. 2009;86(2):323–330.
57. Agblevor FA, Beis S, Mante O, Abdoulmoumine N. Fractional catalytic pyrolysis of hybrid poplar wood. *Ind Eng Chem Res*. 2010;49(8):3533–3538.
58. Mullen CA, Boateng AA, Mihalcik DJ, Goldberg NM. Catalytic fast pyrolysis of white oak wood in a bubbling fluidized bed. *Energy Fuels*. 2011;25(11):5444–5451.
59. Kunii Do, Levenspiel O. *Fluidization Engineering*, 2nd ed. Boston: Butterworth-Heinemann, 1991.
60. Werther J. Fluidized-bed reactors. *Ullmann's Encyclopedia of Industrial Chemistry*. Berlin: Wiley-VCH Verlag GmbH & Co. KGaA; 2000.
61. Levenspiel O. *Chemical Reaction Engineering* (3rd Edition). New York: John Wiley & Sons; 1999.
62. Zhang H, Carlson TR, Xiao R, Huber GW. Catalytic fast pyrolysis of wood and alcohol mixtures in a fluidized bed reactor. *Green Chem*. 2012;14(1):98–110.
63. Geldart D. Types of gas fluidization. *Powder Technol*. 1973;7(5):285–292.
64. Kunii D, Levenspiel O. Fluidized reactor models. 1. For bubbling beds of fine, intermediate, and large particles. 2. For the lean phase - freeboard and fast fluidization. *Ind Eng Chem Res*. 1990;29(7):1226–1234.
65. Mori S, Wen CY. Estimation of bubble diameter in gaseous fluidized-beds. *AIChE J*. 1975;21(1):109–115.
66. Geldart D. Expansion of gas fluidized beds. *Ind Eng Chem Res*. 2004;43(18):5802–5809.
67. Whitaker S. Forced convection heat-transfer correlations for flow in pipes, past flat plates, single cylinders, single spheres, and for flow in packed-beds and tube bundles. *AIChE J*. 1972;18(2):361–371.
68. Cheng Y-T, Huber GW. Production of targeted aromatics by using Diels-Alder classes of reactions with furans and olefins over ZSM-5. *Green Chem*. 2012;14(11):3114–3125.
69. Gidaspow D. *Multiphase Flow and Fluidization*. San Diego: Academic Press, 1994.
70. Jackson R. Locally averaged equations of motion for a mixture of identical spherical particles and a newtonian fluid. *Chem Eng Sci*. 1997;52(15):2457–2469.
71. Anderson TB, Jackson R. A fluid mechanical description of fluidized beds. *Ind Eng Chem Fundam*. 1967;6(4):527–539.
72. ANSYS FLUENT 12.0 Theory Guide. <http://www.ansys.com/ANSYS Inc.>; 2009.
73. Wang JW, van der Hoef MA, Kuipers JAM. Why the two-fluid model fails to predict the bed expansion characteristics of Geldart A particles in gas-fluidized beds: a tentative answer. *Chem Eng Sci*. 2009;64(3):622–625.
74. Wang JW, van der Hoef MA, Kuipers JAM. The role of scale resolution versus inter-particle cohesive forces in two-fluid modeling of bubbling fluidization of Geldart A particles. *Chem Eng Sci*. 2011;66:4229–4240.
75. van Wachem BGM, Schouten JC, van den Bleek CM, Krishna R, Sinclair JL. Comparative analysis of CFD models of dense gas-solid systems. *AIChE J*. 2001;47(5):1035–1051.
76. Lun CKK, Savage SB, Jeffrey DJ, Chepurmy N. Kinetic theories for granular flow - inelastic particles in Couette-flow and slightly inelastic particles in a general flowfield. *J Fluid Mech*. 1984;140:223–256.
77. Johnson PC, Jackson R. Frictional collisional constitutive relations for antigenulocytes-materials, with application to plane shearing. *J Fluid Mech*. 1987;176:67–93.
78. Hull AS, Chen Z, Agarwal PK. Influence of horizontal tube banks on the behavior of bubbling fluidized beds: 2. *Mixing of solids*. *Powder Technol*. 2000;111:192–199.
79. Song XQ, Grace JR, Bi H, Lim CJ, Chan E, Knapper B, McKnight CA. Gas mixing in the reactor section of fluid cokers. *Ind Eng Chem Res*. 2005;44(16):6067–6074.
80. Chyang C-S, Qian F-P, Chiou H-Y. Radial gas mixing in a fluidized bed with a multi-horizontal nozzle distributor using response surface methodology. *Chem Eng Technol* 2007;30(12):1700–1707.
81. Li T, Pougatch K, Salcudean M, Grecov D. Mixing of secondary gas injection in a bubbling fluidized bed. *Chem Eng Res Des*. 2009;87:1451–1465.
82. Blatnik MT. *Optimization of Mixing in a Simulated Biomass Bed Reactor with a Center Feeding Tube*. Amherst: Mechanical Engineering, University of Massachusetts Amherst; 2013.
83. Levenspiel O. *The Chemical Reactor Omnibook*. Corvallis, OR: OSU Book Stores, 1979.
84. Davidson JF, Harrison D, Carvalho J. Liquid-like behavior of fluidized-beds. *Annu Rev Fluid Mech*. 1977;9:55–86.
85. Wen CY, Yu YH. A generalized method for predicting minimum fluidization velocity. *AIChE J*. 1966;12(3):610–612.
86. Levenspiel O. *Engineering Flow and Heat Exchange*. New York: Plenum Press, 1984.
87. Miwa K, Muchi I, Mori S, Kato T. Behavior of bubbles in a gaseous fluidized-bed. *Int Chem Eng*. 1972;12(1):187–194.
88. Davidson JF, Harrison D. *Fluidised Particles*. New York: University Press; 1963.
89. Wallis GB. *One-Dimensional Two-Phase Flow*. New York: McGraw-Hill; 1969.
90. Werther J, Foundation E, Kyōkai KK. *Fluidization IV: Fourth International Conference on Fluidization*. Kashikojima, Japan: Society of Chemical Engineers, May 29–June 3, 1983.
91. Bi HT, Grace JR. Effects of pressure and temperature on flow regimes in gas-solid fluidization systems. *Can J Chem Eng*. 1996;74(6):1025–1027.
92. Pattipati RR, Wen CY. Minimum fluidization velocity at high temperatures. *Ind Eng Chem Process Des Dev*. 1981;20(4):705–707.
93. Abrahamsen AR, Geldart D. Behaviour of gas-fluidized beds of fine powders part I. *Homogeneous expansion*. *Powder Technol*. 1980;26(1):35–46.

Manuscript received Oct. 10, 2013, and revision received Jan. 3, 2014.